Montclair State University

Montclair State University Digital Commons

Theses, Dissertations and Culminating Projects

5-2024

An experimental and computational study on the dynamics of vertical axis wind turbines

Stephen Conte
Montclair State University

Follow this and additional works at: https://digitalcommons.montclair.edu/etd

Part of the Mathematics Commons, and the Oil, Gas, and Energy Commons

Recommended Citation

Conte, Stephen, "An experimental and computational study on the dynamics of vertical axis wind turbines" (2024). *Theses, Dissertations and Culminating Projects*. 1388.
https://digitalcommons.montclair.edu/etd/1388

This Thesis is brought to you for free and open access by Montclair State University Digital Commons. It has been accepted for inclusion in Theses, Dissertations and Culminating Projects by an authorized administrator of Montclair State University Digital Commons. For more information, please contact digitalcommons@montclair.edu.

Abstract

This thesis conducts preliminary analyses on the estimated performance of a novel Vertical-Axis Wind Turbine at a small-scale through experimental and numerical means. This includes the construction of a wind tunnel in the Complex Fluids Lab at Montclair State University for the simulation and analyses of small-scale prototypes of said VAWT; as well as the utilization of Ansys ® 2024 Student Fluent R1 [9] for CFD simulation of scaled single-blade pairs, and potentially full-models of said VAWT.

MONTCLAIR STATE UNIVERSITY

An Experimental and Computational Study on the Dynamics of Vertical Axis Wind Turbines

by

Stephen Conte

A Master's Thesis Submitted to the Faculty of
Montclair State University
In Partial Fulfillment of the Requirements
For the Degree of
Master of Mathematics

May 6, 2024

College of Science and Mathematics

Department of Mathematics

Thesis Committee:

[redacted]

Dr. Ashwin Vaidya

[redacted]

Dr. Arup Mukherjee

[redacted]

Dr. Bogdan Nita

Committee Member

An Experimental and Computational Study on the Dynamics of Vertical Axis Wind Turbines

A THESIS

Submitted in partial fulfillment of the requirements
for the degree of Masters in Mathematics

by

Stephen Conte

Montclair State University

Montclair, NJ

2024

Acknowledgments

I would like to thank Dr. Ashwin Vaidya for his continual guidance and encouragement throughout my time at Montclair State University. He has provided me with mentorship, advice and countless opportunities to further my academic career for which I am truly grateful. There were a number of times throughout this research that I felt out of my depth, but his encouragement helped me to feel content with the work I've produced; Without him, this research would not be possible, thank you Dr. Vaidya. I would also like to thank my committee members, Dr. Arup Mukherjee and Dr. Nita Bogdan for choosing to be apart of my defense committee, and for also being great professors during my time at Montclair. A big thank you to the New Jersey Economic Development Authority (NJEDA) and NJ Wind Institute fort their support and initial funding for this project; as well as Dr. Pankaj Lal and the Center of Environmental Analytics and Clean Energy (CESAC) for their additional funding and support on this research. Of course, thank you to Sevdalin Semov, the creator of the design for the S-WIND VAWT, for providing me with the opportunity to work on such an interesting project.

I would of course like to thank my family for giving me the opportunity to further my academic career and for always supporting me. To my parents, my grandma, my sisters, my great aunt (Tia), my girlfriend Adriana, my dog Maddie, and my friends: I love you all, you mean the world to me and so does your support, thank you!

Contents

Nomenclature

η	Turbine Power Efficiency
γ	Kinematic Viscosity
λ	Tip-Speed Ratio
μ	Dynamic Viscosity
ω	Turbulent Dissipation Rate in k-ω SST turbulence model
$\rho\vec{g}$	Gravitational Body Forces
τ	Torque
$\vec{\omega_t}$	Angular Velocity Vector
$\vec{\vec{\tau}}$	Stress Tensor
$\vec{F}$	External Body Forces
$\vec{r_0}$	Position Vector to origin of moving coord. from global coord.
$\vec{u_r}$	Velocity of moving frame relative to stationary
$\vec{v_r}$	Relative Velocity
$\vec{v_t}$	Linear Velocity Vector
$\vec{v}$	Absolute Velocity Vector

c	Blade Chord Length
c_D	Coefficient of Drag
c_L	Coefficient of Lift
D	Turbine Diameter
F_D	Force of Drag
F_L	Force of Lift
R	Turbine Radius
R_{e_c}	Reynolds' number with characteristic length as c
R_{e_D}	Reynolds' number with characteristic length as D
ρ	Density of Air
AoA	Angle of Attack
DW	Downwind
HAWT	Horizontal-Axis Wind Turbine
LW	Leeward
UW	Upwind
VAWT	Vertical-Axis Wind Turbine
WW	Windward

List of Figures

List of Tables

Chapter 1

Introduction

The global transition towards clean, large-scale energy sources is quickly becoming a reality as many nations pledge to meet promising quotas in the near future. Specifically, the implementation of large-scale wind energy is a rapidly developing industry in both on- and off-shore settings. On January 27, 2021, the United States made considerable steps towards the solidification of a clean-energy future with the introduction of Executive Order 14008, titled *Tackling the Climate Crisis at Home and Abroad*. This order intends to considerably expand off-shore and on-shore renewable energy, with ambitious goals to achieve 30 GW of offshore wind by 2030, and the ability to implement 25 GW of onshore renewable energy by 2025 [29]. These metrics can only be met with efficient scaling and significant considerations for cost, performance and longevity for large-scale turbine implementations [14]. With the assumed desire to generate arrays of these large-scale turbines for maximal power extraction, exploring alternative options to the Horizontal-Axis Wind Turbine (HAWT) may be beneficial. Studies pertaining to the Vertical-Axis Wind Turbine (VAWT) suggest it may have be a valuable consideration for array-configurations and other niche-applications such as low-speed turbulent areas, which has sparked further research interest. This study performs preliminary experimental and numerical studies on a novel VAWT, the S-WIND, created by Sevdalin Semov, with the utilization of small-scale real and simulated model.

Chapter 2

Methodology

2.1 Literature Review

For this study a systematic Literature Review of scholarly articles and reference guides on Vertical Axis Wind Turbines (VAWTs), and simulations of VAWTs utilizing Computational Fluid Dynamics Simulation (CFD) Software was conducted. Most of the collected scholarly articles which performed numerical studies implemented the utilization of Ansys ® Fluent for CFD analyses, specifically for the use of the Sliding Mesh Model (SMM) to simulate turbine performance at varying values of λ, which will be expanded upon in 2.1.2. [20] explored novel helical-blade designs with varying widths for the Savonius turbine in 2D, with a maximal improvements in rotor power-coefficient of $\sim 6\%$. [24] introduced obstacles in front of the returning blades for the Savonius in 2D simulations, noting improvements in typical rotor power-coefficients $\sim 37\%$. They also performed a blade-optimization process for the Savonius, noting an improvement in rotor power-coefficient $\sim 64\%$ relative to the conventional rotor without an obstacle. [1] constructed both 2D and 3D simulations of the Darrieus turbine with straight and helical blades employing the sliding mesh method. A time-step analysis was performed for determination of the optimal selection for transient flow, the optimal selection being 0.01s. [12] performed both experimental and numerical studies of NACA-airfoil type modifications to the Savonius blades, with a comparative classical Savonius for reference. Experimental studies utilized small-scale models within a constructed wind tunnel, and numerical studies employed the 2D sliding mesh model to simulate turbine performance; however both experimental and numerical results exceeded conventional power-estimates for tested values of λ. [27] also performed experimental studies within a constructed sub-sonic wind tunnel utilizing small-scale models of the Darrieus and Savonius, and logged relevant data quantities. Initial project motivations stemmed from previous research on the auto-rotation and energy-harvesting potential of small-scale, 3D-printed cylindrical particles suspended in a flow-tank. The research examined the impact of upstream blockages on particle auto-rotation, concluding that certain arrangements improved particle RPM by $\sim 200\%$ [11]. This is useful as a future consideration for configuration optimization, or as a method of simplifying the necessary experimental and/or simulated domain. VAWTs have historically been overshadowed in commercial settings by HAWTs due to their higher-rated standalone power efficiencies, and historical performance at large-scales. However, the size of the HAWT continues to grow in terms of tower height and blade length, adding further complexity to the scaling process. VAWTs propose certain advantages over conventional HAWTs that brings attention to researchers for specific-applications. VAWTs are omni-directional meaning they are able to capture the wind from any direction, unlike the HAWT which requires complex yaw control systems to ensure the blades are positioned properly [19]. Certain VAWT types have self-starting capabilities and are able to operate 'well' at low-wind speeds relative to HAWTs (albeit at a low-efficiency rating), which makes them good candidates in urban, or low-altitude applications. The following graph displays the efficiencies of various types of turbines, including the two types of VAWTs that will be discussed.

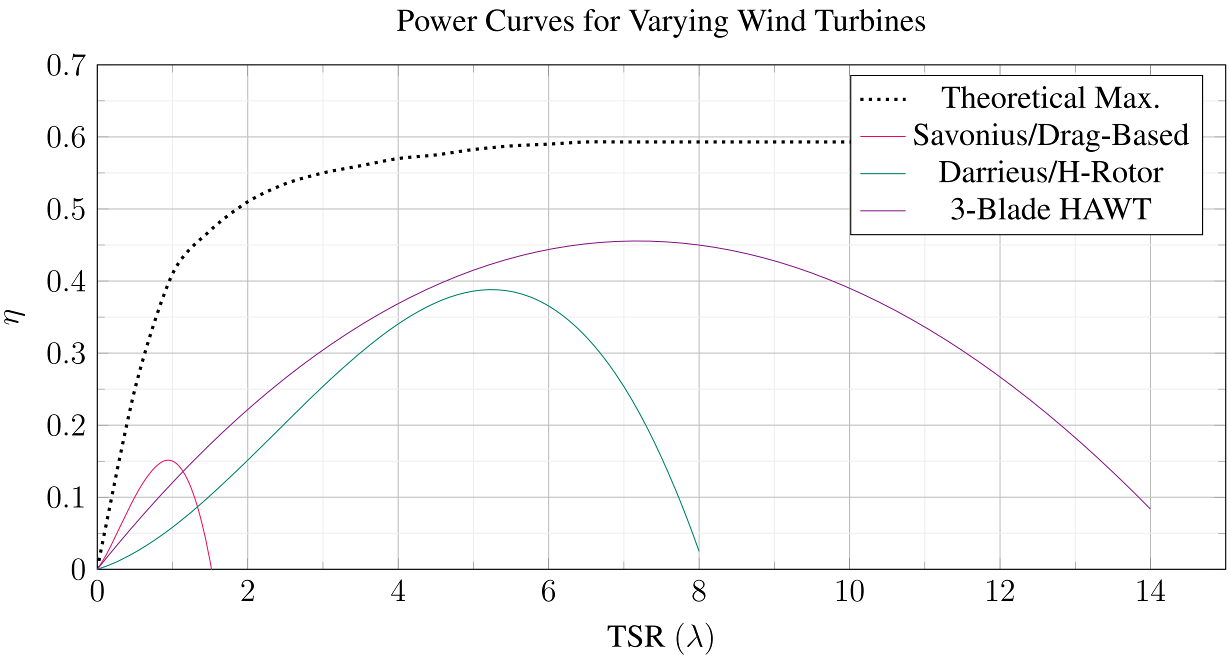

Figure 2.1: Known power coefficient curves for varying wind turbines as a function of tip-speed ratio

Observe that the Savonius Rotor, which is a simple drag-based VAWT, achieves a maximum rotor power coefficient between $[0.1, \sim 0.15]$ according to Figure 2.1. Drag-based VAWTs are considered the least efficient of the VAWTs, because they are unable to reach blade-tip speeds faster than the wind. This is also represented on the graph, whose x-axis is representative of a model's Tip-Speed Ratio (λ), which is further expanded upon in the numerical setup. This can be seen as an advantage in the sense that they are able to operate well at low-speeds and turbulent flows. It is also considered a disadvantage because these configurations lack substantial lift-forces and thus are unable to generate significant power relative to the lift-based VAWTs. It is a niche area of consideration for a standalone model without further optimization, with some literature suggesting the drag-based VAWT is primarily more an area of research for hobbyist or student-interest [28]. Yet other studies, which have extensively explored geometric alterations of the drag-based model and the introduction of upstream blockages have seen considerable increases in rotor power coefficient values up to 0.26 and multi-stage configurations seeing power-coefficients of up to 0.3 [2]. Lift-Based VAWTs are the most efficient of the VAWTs in terms of power production, because of their ability to operate at high-wind and tip-speed. There is research demonstrating Darrieus-type, and H-rotor type-models reaching rotor power coefficients of 0.4 [23].

(a) Savonius (b) Darrieus (c) H-Rotor

Figure 2.2: Varying known types of VAWTS

2.1.1 The S-WIND VAWT

The small-scale S-WIND is a novel VAWT design, and is utilized for testing because of its availability. The model is comprised of pairs of thin, airfoil-like blades which are stacked on top of each-other. Designed by collaborator and industrial designer, Sevdalin Semov, the S-WIND is a hybrid VAWT which utilizes both drag and lift forces to extract energy from the wind. The turbine's motion is largely reliant on the applied wind force to the blade faces on the Upwind (UW) and Leeward (LW) portion; while the Angle of Attack (AoA) alteration mechanism on the

Downwind (DW) and Windward (WW) portion introduces new lift forces which may increase the turbines performance potential. The model has similarities to the Savonius turbine, however is unique in its own respects.

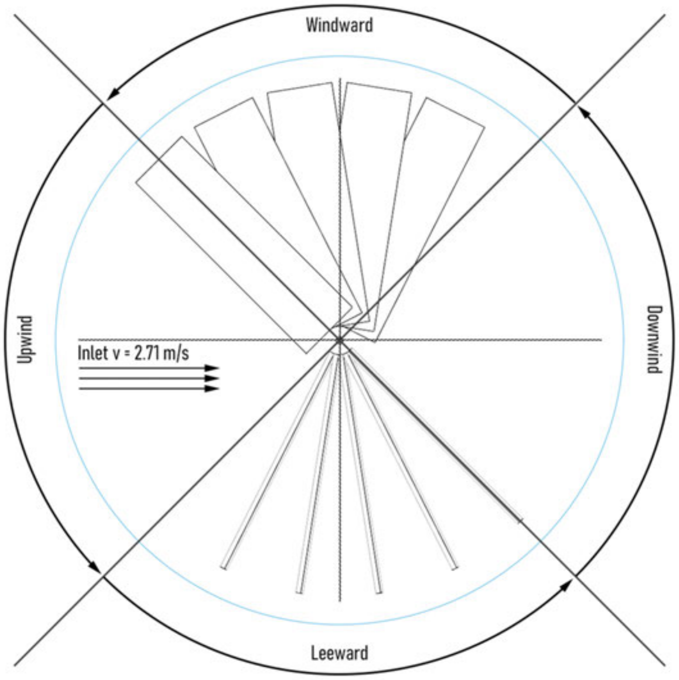

Figure 2.3: Diagram depicting rotational labels for top-view of S-WIND Spiral VAWT revolution

Each blade-pair in the S-WIND turbine has its own auto-rotational capabilities, meaning the turbine has a self-regulating mechanism for the blades' AoA. This mechanism intends to minimize the AoA on the DW and WW portion of its revolution, while maximizing it on the upwind UW and leeward LW portion. This alteration in design modification aims to maximize wind-harvesting potential on the UW and LW portion of the turbine's revolution by maximizing the swept blade area, thus maximizing potential drag and torque. Figures provided by the designer [26] which grant further insight to this concept are displayed:

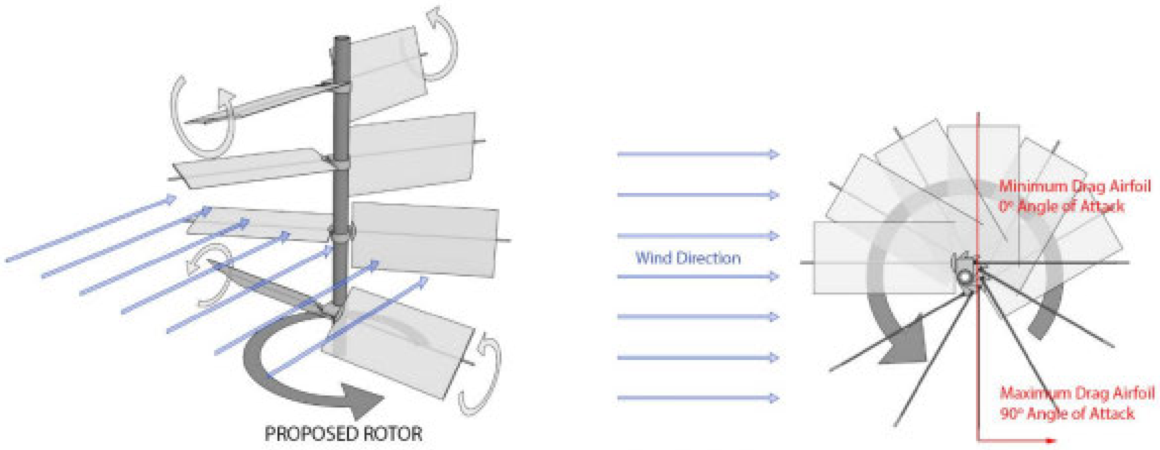

(a) Angled-View

(b) Top-View

Figure 2.4: S-WIND proposed rotor dynamics conceptual image. Thank you to Mr. Semov for preparing and sharing the images with us.

This is a stark contrast to conventional drag-based VAWTs such as the Savonius, which lack blade-pitch alteration mechanisms due to their simple geometries. The addition of an AoA alteration mechanism introduces new potential lift forces, turbulence and wake patterns to be explored and considered. In the experimental set-up, tests will be run on a small-scale prototype of the model provided by the designer. In the numerical set-up, due to software limitations, the simulation of a simplified single blade-pair is explored.

2.1.2 Ansys Fluent Theory

Disclaimer: Ansys ®Fluent is a Commercial software, and thus does not share all of the inner-workings of its methodologies. The majority of the provided information is directly sourced from Ansys ®2024, R1, Fluent Theory and User Guides.

2.1.2.1 Governing Equations

For all flows, Ansys ®Fluent solves the conservation equations for mass and momentum utilizing the Finite Volume Method.

The Conservation of Mass equation is given by:

$$\frac{\partial \rho}{\partial t} + \nabla \cdot (\rho \vec{v}) = 0 \tag{2.1}$$

The Conservation of Momentum in an inertial reference frame is described by:

$$\frac{\partial}{\partial t}(\rho \vec{v}) + \nabla \cdot (\rho \vec{v} \vec{v}) = -\nabla \rho + \nabla \cdot (\vec{\vec{\tau}}) + \rho \vec{g} + \vec{F} \tag{2.2}$$

where ρ is static pressure, $\vec{\vec{\tau}}$ is the stress tensor, and $\rho \vec{g}$ and $\vec{F}$ are gravitational body and external body forces. The stress tensor is provided:

$$\vec{\vec{\tau}} = \gamma[(\nabla \vec{v} + \nabla \vec{v}^T) - \frac{2}{3} \nabla \cdot \vec{v} I] \tag{2.3}$$

where γ is the molecular viscosity, I is the unit tensor, and the second term on the right-hand side (RHS) is the effect of volume dilation [3].

2.1.2.2 Simulating Flow in a Moving Reference Frame

The steady-state case is solved by utilizing the Multiple Reference Frame (MRF) model, which requires establishing the means to simulate flows with moving reference frames. The utilization of a moving reference frame renders a problem that is unsteady from an inertial reference frame steady with respect to the moving frame. Consider a coordinate system translating with a linear velocity $\vec{v_t}$ and rotating with angular velocity $\vec{\omega_t}$ relative to a still reference frame. The origin of the moving system is found through a position vector $\vec{r_0}$, and the axis of rotation is defined by a unit direction vector $\hat{a}$ such that $\vec{\omega} = \omega\hat{a}$:

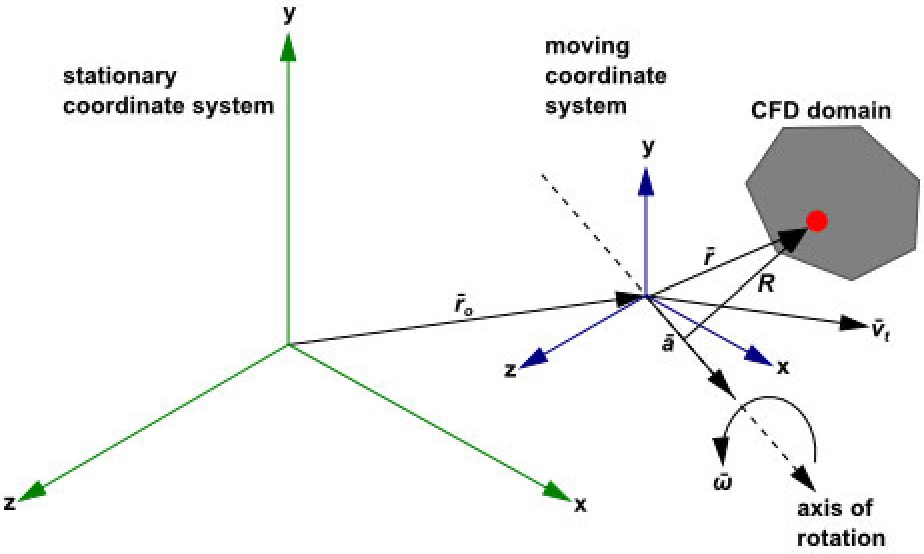

Figure 2.5: Stationary and Moving Reference Frame - Diagram from Ansys ® Fluent 2024 R1 Theory Guide [4]

The computational domain, labeled 'CFD domain' in the above figure, is defined with respect to the moving frame such that any chosen point in the domain is found by position vector $\vec{r}$ from the origin of the moving frame. The fluid velocities are then transformed from the stationary frame to the moving frame using:

$$\vec{v_r} = \vec{v} - \vec{u_r}$$

where

$$\vec{u_r} = \vec{v_t} + \vec{\omega} \times \vec{r}$$

Above, $\vec{v_r}$ is the relative velocity, $\vec{v}$ is the absolute velocity, $\vec{u_r}$ is the velocity of the moving frame relative to the stationary frame, and $\vec{\omega}$ is the angular velocity. Both $\vec{\omega}$ and $\vec{v_t}$ can be functions of time. In the following simulations, there will be no translational frame velocity ($\vec{v_t}$) as the motion of the blades, and non-existent 'hub' are purely rotational. When solving the equations of motion in the moving reference frame, the acceleration is altered by additional terms that appear in the momentum equations.

Absolute Velocity Formulation For the absolute velocity formulation, the governing equations of fluid flow for a steadily moving reference frame are:

Conservation of mass:

$$\frac{\partial \rho}{\partial t} + \nabla \cdot \rho \vec{v_r} = 0 \tag{2.4}$$

Conservation of momentum:

$$\frac{\partial}{\partial t}\vec{v} + \nabla \cdot (\rho \vec{v_r} \vec{v}) + \rho\big[\vec{\omega} \times (\vec{v} - \vec{v_t})\big] = -\nabla p + \nabla \cdot \vec{\vec{\tau}} + \vec{F} \tag{2.5}$$

Conservation of energy:

$$\frac{\partial}{\partial t}\rho E + \nabla \cdot (\rho \vec{v_r} H + p \vec{u_r}) = \nabla \cdot (k \nabla T + \vec{\vec{\tau}} \cdot \vec{v}) + S_h \tag{2.6}$$

Here the Coriolis and centripetal accelerations are simplified to $([\vec{w} \times (\vec{v} - \vec{v_t})])$.

Relative Reference Frame Motion Ansys Fluent allows the specification of a particular frame of motion relative to an already moving (rotating in this case) reference frame [4]. For the purposes of this research this is incredibly useful, since we will attempt to generate a baseline for the model's performance by introducing 2 axes of rotation to the blade-pairs. Here the resulting velocity vector becomes:

$$\vec{v_r} = \vec{v} - \vec{u_r} \tag{2.7}$$

where

$$\vec{u_r} = \vec{u_{r1}} + \vec{u_{r2}} \tag{2.8}$$

and

$$\vec{\omega} = \vec{\omega_1} + \vec{\omega_2} \tag{2.9}$$

2.1.2.3 The Multiple Reference Frame Model

As stated, the Multiple Reference Frame (MRF) model is a steady-state approximation that applies rotational velocities to individual cell zones utilizing the moving reference frame equations. The MRF approach does not take into account relative motion of a moving zone with respect to adjacent zones since the mesh remains fixed for the computation, and only has prescribed rotational frame velocities on its outer rotating regions. For the sake of these computations, the MRF model will be used to compute an initial flow-field that can be used as an initial condition for a number of transient sliding mesh calculations. This calculated initial flow-field will significantly reduce the computational time spent running transient simulations. The absolute velocity formulation is used in our case, meaning that the governing equations in each subdomain are written with respect to the subdomain's reference frame, but the velocities are stored in the absolute frame. This means that no special treatment is required at the interface between two subdomains [4].

2.1.2.4 The Sliding Mesh Model

The Sliding Mesh model is a simplified version of general dynamic mesh motion, and is utilized in this research to estimate turbine performance under transient conditions. The general conservation equation for dynamic and sliding meshes is nearly equivalent, the only exception being that mesh motion in the sliding mesh is rigid. Meaning there is no alteration of the original shape or volume of the cells. This will simplify the governing equations of the dynamic mesh considerably [5]. The integral form of the conservation equation for some scalar, ϕ, on an arbitrary control volume, V, whose boundary is moving can be written as:

$$\frac{d}{dt}\int_V \rho\phi\, dV + \int_{\partial V} \rho\phi(\vec{u} - \vec{u_g}) \cdot d\vec{A} = \int_{\partial V} \Gamma\nabla\phi \cdot d\vec{A} + \int_V S_\phi\, dV \tag{2.10}$$

where ρ is the fluid density, $\vec{u}$ is the flow velocity vector, $\vec{u_g}$ is the mesh velocity of the moving mesh, Γ is the diffusion coefficient, and S_ϕ is the source term of ϕ. Now, again with a sliding mesh, since the cell shape and volume are not altered, the time rate of change of the cell volume is zero. Thus the $(n+1)^{th}$ time level volume, $V^{n+1} = V^n$. and the time derivative term in Equation (2.10) becomes:

$$\frac{d}{dt}\int_V \rho\phi\, dV = \frac{[(\rho\phi)^{n+1} - (\rho\phi)^n]V}{\Delta t} \tag{2.11}$$

2.1.2.5 Turbulence Modeling

General Principles Using Reynolds averaging, the solution variables of the exact Navier-Stokes equations are simplified to their mean time-averaged and fluctuating components:

$$u_i = \vec{u_i} + u_i^{'}$$

where $\vec{u_i}$ and $u_i^{'}$ are the mean and fluctuating velocity components; and likewise for pressure or other scalars:

$$\varphi = \vec{\varphi} + \varphi^{'}$$

where φ denotes said scalar. Substituting these expressions for the flow variables into the instantaneous continuity and momentum equations and taking a time-average constructs the Reynolds-Averaged Navier-Stokes (RANS) equations. Additional terms that appear are that of turbulence [6].

$$\frac{\partial \rho}{\partial t} + \frac{\partial}{\partial x_i}(\rho u_i) = 0 \tag{2.12}$$

$$\begin{gathered} \frac{\partial}{\partial t}(\rho u_i) + \frac{\partial}{\partial x_j}(\rho u_i u_j) = \\ -\frac{\partial p}{\partial x_i} + \frac{\partial}{\partial x_j}[\gamma(\frac{\partial u_i}{\partial x_j} + \frac{\partial u_j}{\partial x_i} - \frac{2}{3}\delta_{ij}\frac{\partial u_i}{\partial x_i})] + \frac{\partial}{\partial x_j}(-\rho \vec{u_i^{'} u_j^{'}}) \end{gathered} \tag{2.13}$$

Selected Turbulence Model The Shear-Stress Transport (SST) k-ω [22] turbulence model is the selected turbulence model by default in [9] and will be utilized for this research because of its specific accuracy and applicability to adverse pressure gradient flows, and airfoil-flows [6].

2.2 Experimental Setup

Pre-CFD studies involved experimentation on a small-scale prototype of the novel S-WIND VAWT, dimensions are provided below.

# of Blades	Length [m]	Height [m]	Blade Width [m]
10	0.4572	0.4508	0.008
8	0.4572	0.3670	0.008
6	0.4572	0.2832	0.008

Figure 2.6: S-WIND VAWT experimental small-scale model dimensions

Experiments conducted in the Complex Fluids Lab at Montclair State University focused on gathering quantitative performance data on differing configurations of the novel VAWT for comparative analyses. A wind-tunnel was designed using Autodesk Fusion Student 2024 [18] and then constructed within the lab. Autodesk Fusion © 2024 is a free, popular CAD software which is utilized in this research for blade design. The purpose of the wind tunnel being to capture data on the turbine to model its behavior under isolated conditions, this is a similar concept to the flow-tank utilized in [30], [11]. The construction of a wind-tunnel for small-scale model analyses is also completed (using more structured material) within [27], [12]. The following figure provides a visual for the Fusion360-designed tunnel, the constructed tunnel, and a table of the dimensions for reference.

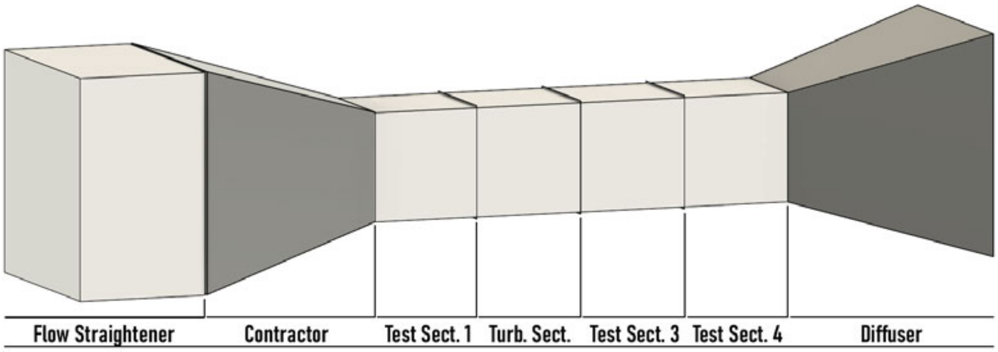

(a) Fusion360-created tunnel design

(b) Constructed wind tunnel

Figure 2.7: Wind tunnel design and construction

Tunnel Component	Length (m)	Width (m)	Height (m)
Flow Straightener	0.61	1.03	1.03
Contractor/Diffuser	0.95	1.03	1.03
(4) Test Sections	0.51	0.51	0.51
Total Tunnel Dimensions	4.15	2.07	2.07

Table 2.1: Wind tunnel dimensional information

To simulate wind-flow, a Dayton 2-Speed Light-Duty Industrial Fan is placed at the front-end of the tunnel. A measuring tape is laid on the table and a number of fan distances are chosen as a method of simulating different wind speed conditions. Wind speeds are captured by placing a continuous data-logging anemometer at the listed distances and capturing the wind speed for a 4-minute time interval, with the intention of reducing fan speed fluctuations.

Distance (ft.)	Distance (m)	Avg. Speed 1 (m/s)	Avg. Speed 2 (m/s)
1	0.31	5.94	7.09
3	0.91	5.47	6.67
6	1.83	4.02	4.7
7 (Tunnel)	**2.13**	**3.27**	**3.91**
9	2.74	2.51	3.11
12	3.66	2.27	2.71

Table 2.2: Dayton fan average speed estimates at varying distances

The bolded distance with the ’Tunnel’ label is listed as such because it is distance of the model from the fan. It is utilized in this experiment as an estimated measurement of isolated turbine performance. Thus, within the wind tunnel the performance of the novel VAWT is evaluated with inlet velocity values of (3.27 m/s, 3.91 m/s). As can be seen in Figure 2.7(b), a portion of the turbine’s tower protruded from the top of its wooden enclosure, where a gearwheel connected the tower to a 300V, 0.128A DC motor via a belt. The motor connected to a 1600V, 100A rated 3-phase actuator, from which instantaneous voltage and current values were extracted from. The following tools were utilized in performance data collection:

(a) SHIMPO DT-2100 Contact Tachometer (b) BTMETER BT-90EPC Digital Multimeter (c) Protmex Digital Anemometer

Figure 2.8: Data collection tools

These were used to capture continuous values for the following metrics in tool-listed order: RPM, Voltage, Current, and Wind Speed. The provided blades for the small-scale model were modular, meaning experimentation across multiple configurations with differing blade numbers and rotational angles was feasible. Blade-pair angular spacing was altered and labeled as θ_p. The configurations we report on in this thesis are described in Table 2.3. Due to size constraints of the wooden enclosure, the maximum number of functional blade-pairs was chosen to 5. Thus the following 9 configurations were assessed:

Config./Blade #	6B	8B	10B
Spiral	Spi-6B	Spi-8B	Spi-10B
Staggered	Stg-6B	Stg-8B	Stg-10B
Parallel	Prl-6B	Prl-8B	Prl-10B

Table 2.3: Blade configurations to be tested

(a) Parallel; $\theta_p = 0°$ (b) Spiral; $\theta_p = 45°$ (c) Staggered; $\theta_p = 90°$

Figure 2.9: Small-scale VAWT tested blade configurations

An important setup characteristic is the Reynolds' number of the system, which can be calculated in one of two ways, both are considered:

$$R_{e_D} = \frac{\rho v D}{\mu}$$

or

$$R_{e_c} = \frac{vc}{\gamma}$$

where μ is the dynamic viscosity of air, γ is being defined as the kinematic viscosity of air, D is the turbine diameter, and c is the chord length. In the experimental setup, the velocity ranges between (3.27 m/s, 3.91 m/s), and thus the following ranges of relative Reynolds' numbers are calculated:

$$R_{e_D} = (\sim 102350, \sim 122382)$$

or

$$R_{e_c} = (\sim 1792, \sim 2142)$$

.

2.3 Numerical Setup

Autodesk Fusion © 2024 Student and Ansys ®Fluent Student 2024 R1 were utilized to conduct this study. Ansys ® Fluent Student 2024 R1 contains a number of modules essential for this research: Ansys ® DesignModeler (for geometry setup), Ansys ® Meshing and Ansys ® Fluent. It is important to note that under the student license of Ansys, CFD meshes are limited to 1,048,000 elements; thus the scope of this research is limited by the maximum number of mesh elements.

2.3.1 Single-Blade Pair Configurations

Prior to the simulation of a multi-blade pair configuration, we consider the capabilities of a fully-functional single blade-pair of the novel VAWT model. This first involves the creation of a 3D digital model with the use of Autodesk Fusion [18]. Although it is desired to compare overall turbine performance across different turbine configurations, it is important to begin with a simpler problem, and build towards a more complex one.

(a) $(2', 0.5', 0.076') \equiv (0.6096m, 0.1524m, 0.023m)$

(b) $(1', 1', 0.076') \equiv (0.3048m, 0.3048m, 0.023m)$

(c) $(1.5', 0.667', 0.076') \equiv (0.4572m, 0.2032m, 0.023m)$

(d) $(1.625', 0.75', 0.076') \equiv (0.4953m, 0.2286m, 0.023m)$

Figure 2.10: Fusion360-generated blade profiles

Each blade has a frontal face area of $1ft^2 \equiv 0.0929m^2$. By observing performance differences across varying blade profiles for a single-blade pair, inferences can potentially be made for a selection in multi-blade pair configurations. As noted from the experimental study, blade (a) is the original blade profile for the model, but for CFD purposes its dimensions (along with those of the remaining blade profiles) have been scaled. The swept area of the experimental model was far too small such that it would not produce viable Wattage at the range of wind speeds to be observed in this study. The geometries are exported as STEP files, and imported into the ANSYS ®Workbench's DesignModeler Module [8]. This module was used to begin the model's preparation for simulations. The setup for one blade pair profile will be displayed, because the process for the other geometries was virtually the same and would otherwise be redundant and take up significant space in this section.

2.3.1.1 DesignModeler Setup

The exported blade-profile's STEP file was imported into [8], since the original importation was only a single blade, it was mirrored. From the top navigation bar, the following process was completed (across all blade-profiles): Create → Body Transformation → Mirror was selected; The YZ-plane was chosen as the mirror plane, and the imported single blade as the body. The newly-mirrored blade must be rotated, again the process performed was: Create → Body Transformation → Rotate; The mirrored-blade was selected as the body of interest, and the Normal Axis was selected. Lastly Angle $\theta = 90^{\circ}$ was set and the geometry was generated for the last time. A single-blade pair was constructed.

The rotating region and wind tunnel are created. Beginning with the former; the process was completed as follows: the sketching toolbar was selected and a half circle was created around the XY-plane. The Revolve transformation was selected under Create, utilizing selections of the half circle sketch and the Y-Axis; the Operation was set to 'Add Frozen', and Angle selected as $\theta = 360^{\circ}$. The body was labelled appropriately as 'rr'. This is the created spherical region which surrounded the blade-pair to be rotated. For the simulation of the blades' rotation about their own axes, the Revolve Operation was duplicated, creating a new sphere, the new sphere was scaled by a factor of 1.25 and labeled 'fr'. Lastly, A wind tunnel was created about the XY-plane via a new sketch. A rectangle was created that enclosed the rotating region, then the trim tool was utilized to remove the inlet edge. A half circle was created by the same methodology in place of the original inlet edge. The sketch was then extruded using the Extrude transformation, ensuring Operation was ’Add Frozen’, Direction was ’Both - Symmetric’, Depth was 2m; this body was labelled wt.

Finally, a Body of Influence was created near the region surrounding the blades. The Body of Influence acts as a mesh refinement region, it was utilized to reduce element sizing within its enclosed volume thereby improving mesh quality in the desired region. Thus by it enclosing the swept area of the blades along with a small portion of the far-field, the intentions were to extract more accurate values and contours of interest. The YZ-plane was chosen and a new sketch was created, the rectangle tool was used to enclose the blades and far-field portion. Dimensions and Constraints were added to all created sketches and are displayed. Thus the following sketches have been created with the following properties, along with their correspondingly constructed Bodies:

Sketch	Dimension(s)	Constraint(s)	Created Body	Extrusion Distance
rr-sketch	D: 2m	N/A	rr, fr	-
wt-sketch	H4: 6m, V3: 6m, V5: 3m	Symmetry: Y-Axis	wt	2m
boi-sketch	H11: 0.25m, H9: $0.83\overline{3}$m	Symmetry: Y-Axis	boi	0.7m

Table 2.4: Sketch information table

The final operations performed in DesignModeler were the Boolean-Subtraction Operations, which involved the removal of specified volumes from chosen geometries. This ensured proper interface zones were created and labeled between the wind tunnel, rotating region, and blades.

Boolean	Target Bodies	Tool Bodies	Preserve Tool Bodies (Y/N)
wt-bool	wt	rr	Y
rr-bool	rr	fr	Y
fr-bool	fr	bl, br	N

Table 2.5: Boolean-operations table

It is again important to note that the values provided are specific to the geometric setup for blade profile (a). However the overall process of setting up the geometry, creating the regions, applying appropriate body transformations, dimensions, constraints and creating boolean operations remains the same across all blade profiles. The final geometric setup in DesignModeler, and a visual reference for the listed dimension in Table 2.4 are shown:

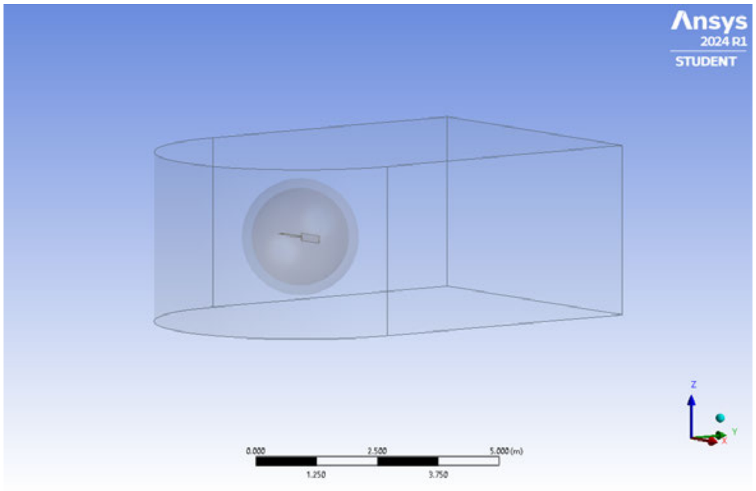

(a) Wind Tunnel Angled-View

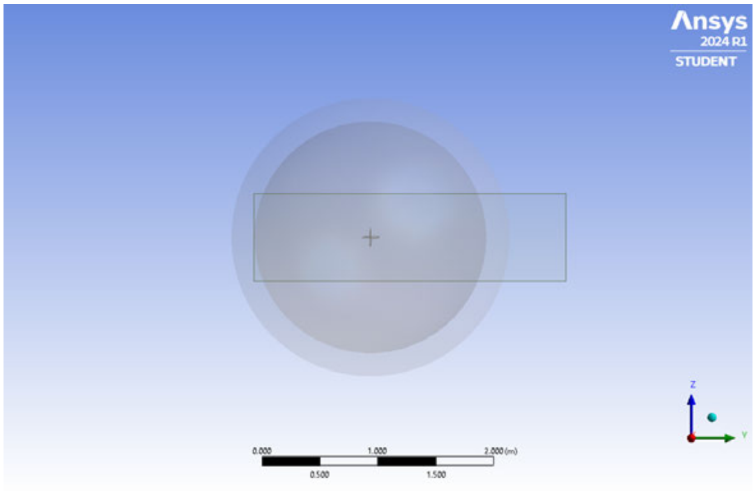

(b) Rotating Region + Body of Influence Side-View

Figure 2.11: Blade Profile (a) Geometric Setup

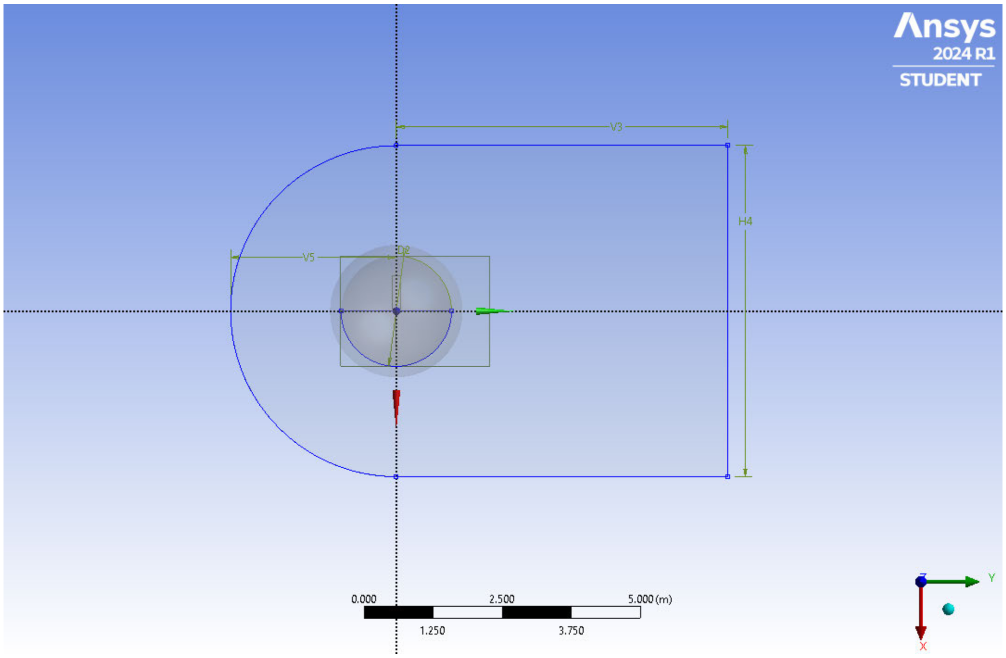

Figure 2.12: Blade-profile (a) geometry dimensional-view

Figure 2.9 provides visual clarification on the dimensions listed in Table 2.4. Here, the labeled dimensions are visually as follows: V3 = 6m depicts the length of the far-field from the X-axis relative to the figure, H4 = 6m depicts the width of the wind tunnel, and V5 = 3m represents the distance of the inlet from the model.

2.3.1.2 Mesh Setup

The DesignModeler geometry was imported into a new Mesh module. Under the Project Tree, the Mesh is selected, the Physics Preference was changed to 'CFD' and the Solver Preference was changed to 'Fluent'. The final mesh after all refinements were applied consists of $216,893$ nodes and $993,394$ elements. Across all blade-profiles, including the Savonius, the number of mesh elements respectively for (G1, G2, G3, G4, Sav.) was (993394, 1013399, 996822, 994322, 1036949). The following settings were applied to this specific geometry to enhance overall mesh quality:

Body of Influence Settings The default element size for the entire fluid domain was reduced to $0.4m$. The created body of influence was setup appropriately as instructed in the User's Guide [10], with the target bodies being: the flap, rotating-region, and wind tunnel, and the element size being $4.5 \cdot 10^{-2}\, m$.

Blade Edge & Face Refinement For blade-profile (a)[1], all blade edges (32) were selected, and were reduced to an element size of $1.8 \cdot 10^{-3}\, m$, with the Behavior set to Soft. All blade faces (18) were selected, and were reduced to an element size of $1 \cdot 10^{-2}\, m$, with the Behavior set to Hard. Additionally applied to the blade faces were 15 maximum layers of Inflation utilizing the First Layer Thickness method. The growth rate remained the default value of 1.2, and the First Layer Height was set as $1 \cdot 10^{-4}\, m$.

---

[1] and all other blade-profiles.

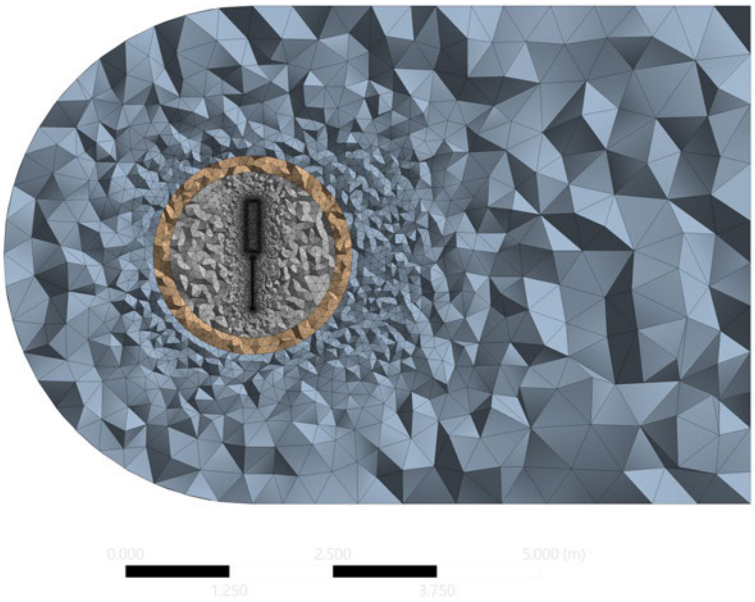

(a) Wind tunnel mesh XY-section plane top-view

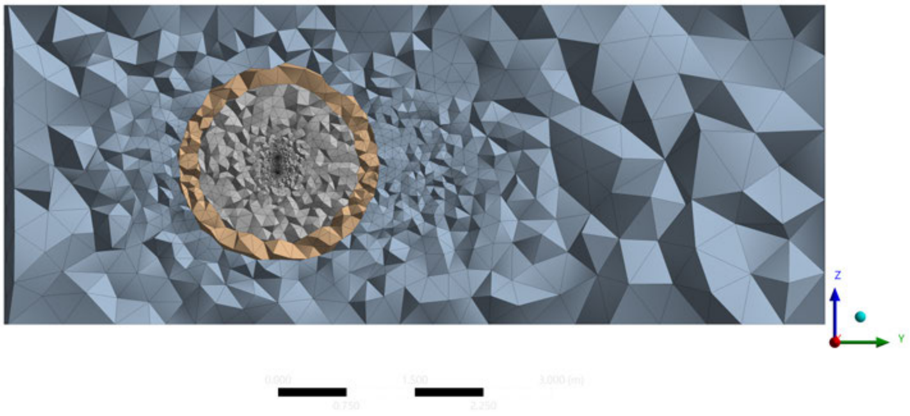

(b) Wind tunnel mesh YZ-section plane side-view

Figure 2.13: Wind tunnel - blade-profile (a) mesh setup

Figure 2.11 shows the mesh refinement surrounding the rotating and flap regions. Figure 2.12a displays a cross section about the YZ-plane of the entirety of the fluid domain, which depicts additional mesh refinement in areas of the wind tunnel surrounding the rotating regions, due to the applied body of influence.

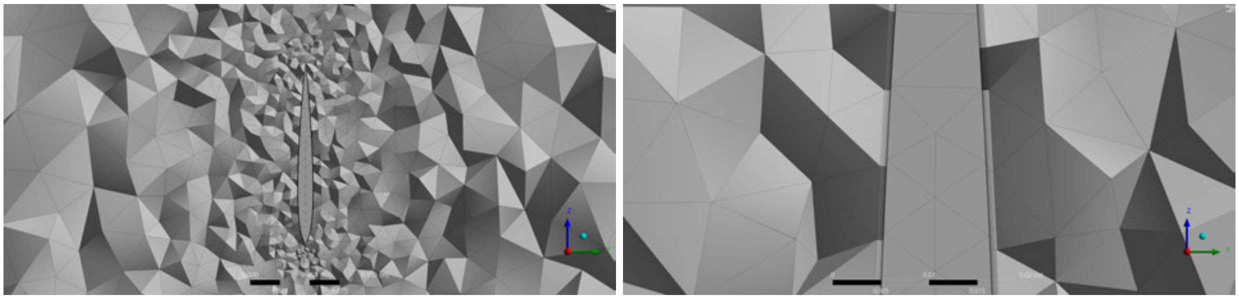

(a) Blade Mesh YZ-Section Plane Side-View (b) Blade Inflation Layer Side-View

Figure 2.14: Rotating/Flap region - Blade-profile (a) mesh setup

Figure 2.11 shows the mesh refinement around the blade region due to the applied body of influence, edge and face sizing, and first inflation layer thickness sizing. With the mesh appropriately constructed for simulation, select 'Update' to transition the mesh to Fluent.

2.3.1.3 Fluent Setup (Steady-State)

The Mesh was imported into the Fluent module, 'Double Precision' was enabled, and the Number of Processes was set to 4. Under 'Setup', the following settings were set for the Steady-State simulation utilizing the MRF model:

Turbulence Model The 3D flow-field is viscous and in-compressible. As discussed, the Shear Stress Transport (SST) k-ω model is chosen for its vast applicability to a number of flows and common usage in similar studies. Here k is the turbulent kinetic energy, and ω (in this sense) is the turbulent specific dissipation rate.

Cell-Zone Conditions There are 3 cell-zones, all of which are fluids and they have the following settings:

Cell-Zone	Motion	Relative to	Origin (x,y,z)	Axis	ω [rad/s]
wt (Wind Tunnel)	n/a	n/a	n/a	n/a	n/a
rr (Rotating Region)	Frame	Absolute	(0,0,0)	(0,0,1)	1.3336614
fr (Flap Region)	Relative Frame	rr	(0,0,0)	(1,0,0)	0.66683071

Table 2.6: Blade-profile (a) Fluent cell-zone conditions $v = 2.71m/s$ &$\lambda = 0.6$

Flap Region velocities (ω_2) were chosen to be $\frac{\omega}{2}$ to maintain minimal AoA on the UW and WW portion of the turbine's revolution as theoretically proposed. Alterations to flap-region velocity should be considered for future studies to be a more precise calculation rather than a constant prescribed motion, as this is only a preliminary choice to model the design's proposed behavior.

Boundary Conditions Provided below are the settings for the simulation's boundary conditions; Interfaces are automatically accounted for by Ansys ®Fluent Student after appropriately labeling named selections in the Mesh module.

Boundary	Type	Specification Method	Magnitude [m/s] or [Pa]
Inlet	Velocity	Magnitude, Norm. to Bound.	2.71 m/s
Outlet	Pressure	Magnitude, Norm. to Bound.	0 Pa

Table 2.7: Blade-profile (a) Fluent boundary conditions

Reference Values Below are the provided reference values for blade-profile (a), the settings are virtually the same across the remaining blade-profiles, with the only variation being 'Length' since the configurations differ in their radii and diameters. The pressure of 0 found in Table 2.8 depicts the prescribed wind-tunnel outlet pressure.

Attribute	Value
Area:	$0.583727\ m^2$
Density:	$1.225\ kg/m^3$
Length:	$1.2192\ m$
Pressure:	$0\ Pa$
Temperature:	$288.16\ K$
Velocity:	$2.71 m/s$
Viscosity (μ):	$1.7894 * 10^{-5};\ kg/(ms)$

Table 2.8: Blade-profile (a) Fluent reference values

Methods Provided is a table with the selected solution methods, this also remains constant among differing blade-profiles.

	Selection
Scheme:	Coupled
Flux Type:	Rhie-Chow: momentum-based

Table 2.9: Blade-profile (a) Fluent Pressure-Velocity Coupling settings

	Selection
Gradient:	Least Squares Cell Based
Pressure:	Second Order
Momentum:	Second Order Upwind
Turbulent Kinetic Energy:	Second Order Upwind
Specific Dissipation Rate:	Second Order Upwind
Pseudo Time Method:	Global Time Step

Table 2.10: Blade-profile (a) Fluent Spatial Discretization settings

Residuals Residuals are the functions of the error in a given solution. More specifically, they are representations of imbalances in the listed quantities of the Conservation equations. It essentially gives information on the status of the solution's convergence based on the specified simulation criteria. All residuals are plotted and displayed below for the converged steady-state MRF solution, all absolute criteria were set to $1 \cdot 10^{-5}$; 700 iterations are run:

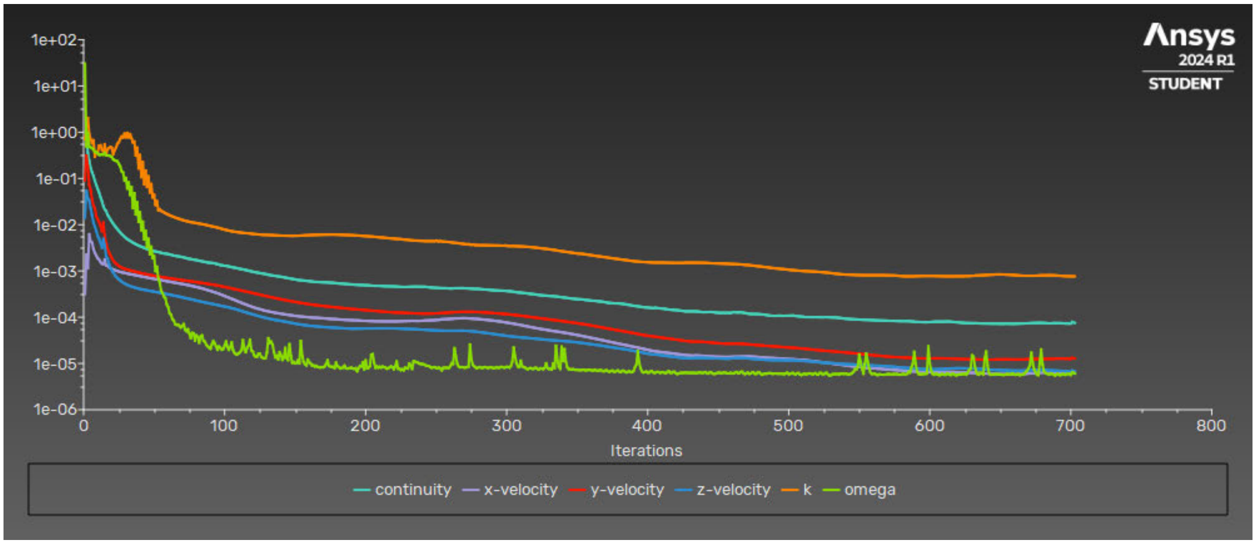

(a) Steady-state residuals

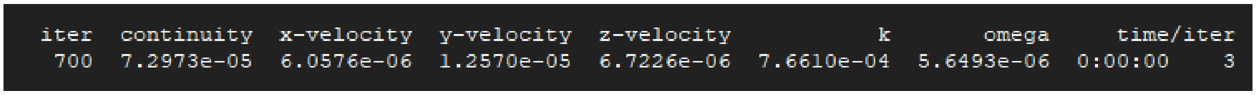

```
  iter  continuity  x-velocity  y-velocity  z-velocity           k       omega     time/iter
   700  7.2973e-05  6.0576e-06  1.2570e-05  6.7226e-06  7.6610e-04  5.6493e-06  0:00:00    3
```

(b) Final iteration residual values

Figure 2.15: Blade-profile (a) - Utilized MRF steady-state solution

Initialization & Run Calculation Again, the utilization of the steady-state case is to apply a converged steady-state solution as an initial flow-field for the transient setup. Hybrid Initialization is utilized with the first 10 iterations matching the selected convergence criteria. 700 iterations are run at an automatic time step method, a conservative length scale method, and a time scale factor of 1.

2.3.1.4 Fluent Setup (Transient)

The previously constructed Steady-State Fluent case in Ansys ®Workbench is selected, duplicated, and then the original solution is dragged from the steady-state case into the duplicated Fluent module's solution cell. This initializes our transient flow-field utilizing the MRF solution as suggested in [4]. After loading the duplicated Fluent module, under General Settings, Solver-Time is swapped from 'Steady' to 'Transient'. Under Cell Zone Conditions, the prescribed Frame Motion is copied to the Rotating and Flap Regions as Mesh Motion. All other settings between the Steady-State and Transient simulation set-ups remained the same.

Residuals The figures below demonstrate the transient residuals for the Sliding Mesh simulation of blade-profile (a) @ $v = 2.71m/s$ and $\lambda = 0.6$:

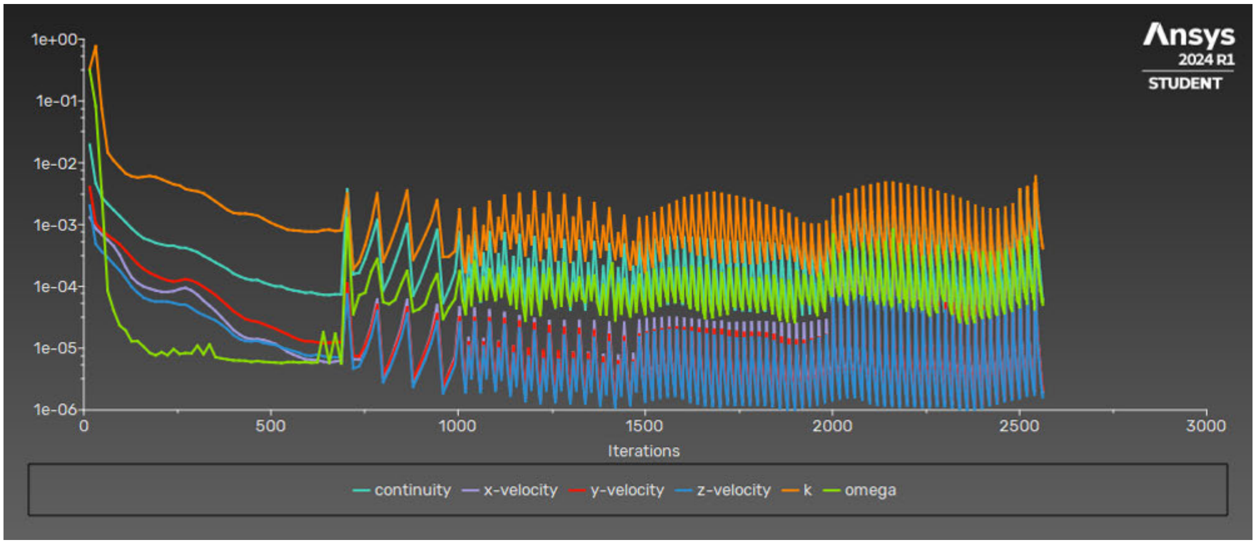

Figure 2.16: Blade-profile (a) - Transient residuals that display the periodic imbalances of listed quantities within the Conservation equations at varying blade AoAs.

2.3.2 Quantities of Interest

To quantify turbine performance there are a number of variables and expressions to solve relative to the simulation parameters. Most importantly of course, is the determining preliminary estimates of power efficiency and power generation. Both of which are a direct result of produced torque on the blades. The calculation for efficiency considers the capabilities of the respective turbine as a ratio of the actual produced turbine power over the maximum potential produced power. Thus, we consider:

$$\text{Turbine Power} \coloneqq P_t = \tau\omega$$

and

$$\text{Max. Available Wind Power} \coloneqq P_w = \frac{1}{2}\rho A v^3$$

meaning that,

$$\text{Turbine Power Efficiency} \coloneqq \eta = \frac{P_t}{P_w} = \frac{\tau\omega}{\frac{1}{2}\rho A v^3}$$

η is averaged across a 3-revolution moving average to reduce fluctuations in solution values, providing an estimate for said configuration's performance, while attempting to minimize required simulation time.

In the above, τ is the produced torque on the blades relative to ω, the prescribed rotational velocity of the rotating region containing the blades. ρ is the density of air, $A = 2\pi r h$ is the swept area of the turbine (which is considered to be the surface area of a cylinder body), and v is the inlet velocity. This swept area A also matches the Area found later in Table X, which is utilized to estimate coefficients of drag, and lift. These values are automatically calculated by Fluent after inputting the appropriate values, however their formulas are provided for reference.

$$\text{Coefficient of Drag} \coloneqq C_D = \frac{2F_D}{\rho v^2 A}$$

$$\text{Coefficient of Lift} \coloneqq C_L = \frac{2F_L}{\rho v^2 A}$$

$$\text{Force of Drag} \coloneqq F_D = \frac{1}{2}\rho v^2 C_D A$$

$$\text{Force of Lift} := F_L = \frac{1}{2}\rho v^2 C_L A$$

Again the Reynolds' Number was considered in the numerical setup, with the inlet velocity being 2.71 m/s. The chord Reynolds' number for the system was:

$$R_{e_c} = \frac{vc}{\gamma} = \frac{(2.71\ \text{[m/s]})(0.023\ \text{[m]})}{1.46 \cdot 10^{-5}\ [m^2\text{/s]}} \approx 4269$$

The diameter Reynolds' number across the 5 systems with varying blade-profiles include:

$$R_{e_D}(G1) = \frac{\rho v D}{\mu} = \frac{(1.225\text{kg/}m^3])(2.71\ \text{m/s})(1.2192\ \text{[m]})}{1.7894 \cdot 10^{-5}\ \text{[kg/(ms)]}}) \approx 226192$$

$$R_{e_D}(G2) = \frac{\rho v D}{\mu} = \frac{(1.225\text{kg/}m^3])(2.71\ \text{m/s})(0.6096\ \text{[m]})}{1.7894 \cdot 10^{-5}\ \text{[kg/(ms)]}}) \approx 113096$$

$$R_{e_D}(G3) = \frac{\rho v D}{\mu} = \frac{(1.225\text{kg/}m^3])(2.71\ \text{m/s})(0.3048\ \text{[m]})}{1.7894 \cdot 10^{-5}\ \text{[kg/(ms)]}}) \approx 56548$$

$$R_{e_D}(G4) = \frac{\rho v D}{\mu} = \frac{(1.225\text{kg/}m^3])(2.71\ \text{m/s})(1.143\ \text{[m]})}{1.7894 \cdot 10^{-5}\ \text{[kg/(ms)]}}) \approx 212055$$

$$R_{e_D}(Sav) = \frac{\rho v D}{\mu} = \frac{(1.225\text{kg/}m^3])(2.71\ \text{m/s})(0.8128\ \text{[m]})}{1.7894 \cdot 10^{-5}\ \text{[kg/(ms)]}}) \approx 150795$$

Another important metric that will be useful in performance analyses is a turbine's Tip-Speed Ratio, which is the ratio of the tangential speed of the tip of the blades relative to the actual wind speed. It is an important metric in the consideration of performance conditions for a given turbine configuration and is utilized extensively in any comparative wind turbine study.

$$\text{Tip-Speed Ratio (TSR)} := \lambda = \frac{\omega R}{v}$$

It is commonly known from the literature that drag-based turbines operate at low TSRs ($0 \leq \lambda \leq 1$). Thus it is relevant to provide estimates for a given geometry's power curve by simulating its performance differences at varying operating speeds within an expected range. Thus, a set of TSRs[2] to be tested, will consist of:

$$\lambda_i = (0.3, 0.6, 0.9, 1.2)$$

From the gathered results, extrapolation methods are then used to create desired power curves. As a reminder, ω is a prescribed constant rotational velocity, meaning these turbines are rotating as a result of the prescribed ω; i.e. this is not flow-driven simulation and only a preliminary estimate for both true operating conditions and power. Flow-driven simulations are more time-consuming and computationally demanding and will be discussed as a further consideration for future work.

---

[2] $\lambda_3 = 1.2$ is only tested for specified geometries.

Chapter 3

Results

3.1 Experimental Results

A large portion of the experimental results consisted of capturing unloaded and loaded[1] RPM data across varying configurations of blade numbers, at different simulated wind speeds. Additionally, separate measurements were done to measure generated voltage and current produced by the turbine when performing under-load to find estimates for power of the small-scale model. Of the gathered data, the most 'useful' data points would be the loaded RPM performance within and outside of the wind-tunnel to determine which configuration would perform most 'optimally' under isolated conditions.

Upon introductory analysis of the model at the varying proposed configurations, the parallel configuration was found to experience a dead-zone after the initial wind impact which results in frequent stalling at the slower, more turbulent wind speeds. The dead-zone occurs when the blades are parallel to the wind-flow. This is due to the nature of the parallel configuration; by applying no angular spacing between blade pairs, the turbine's capabilities are limited by the lack of blade coverage per half-revolution, which results from a lack of a substantial wind force to keep the

---

[1] (Un)loaded meaning with(out) attachment to a motor i.e. load.

blades in motion. Thus the Parallel configuration was disregarded early in the studies as a non-optimal configuration, and the focus was shifted solely to the Spiral and Staggered configurations. A diagram was constructed to further explain this concept and will be used to explain the reasoning for the Parallel configuration's dismissal. Note that this diagram considers only half of the top-view for a full model, given that the minimal angle of attack blades are not considered in the diagram.

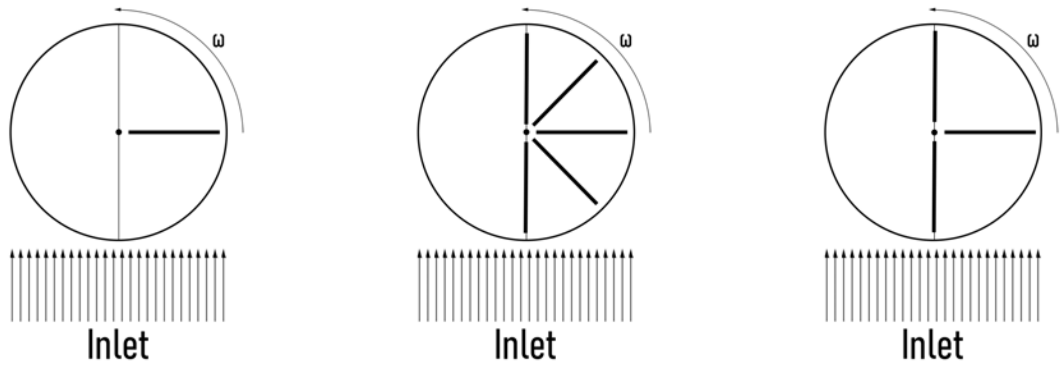

(a) Parallel ($\theta = 0°$) (b) Spiral ($\theta = 45°$) (c) Staggered ($\theta = 90°$)

Figure 3.1: Experimental blade configuration top-view

Having the blades stacked on top of each-other in Figure 3.1(a) results in a turbine whose motion is entirely reliant on the single initially large drag force produced per half-revolution from the sweep of the blades. In contrast, Figures 3.1(b) and 3.1(c) induce angular spacing between blade pairs at different heights about the Z-axis, allowing for additional points of contact per half-revolution, providing additional force (albeit of a lower magnitude than the large force produced by the Parallel configuration) which keeps the turbine in a slower but more consistent motion relative to the Parallel.

3.1.1 Loaded RPM

The loaded RPM measurements that were recorded were at the estimated wind speeds within the wind tunnel i.e. $V_{tun} = (3.27\ m/s,\ 3.91\ m/s)$; however all blade numbers and considered blade configurations originally proposed are still considered. We will first consider differences within configurations at varying blade numbers, and then we will average said values to acquire a more easily understandable graph-set.

3.1.1.1 Spiral

The following graphics display the measured loaded RPM for the Spiral configuration of the novel VAWT with 10, 8 and 6 blades, and at the 2 varying fan-speeds $\in V_{tun}$.

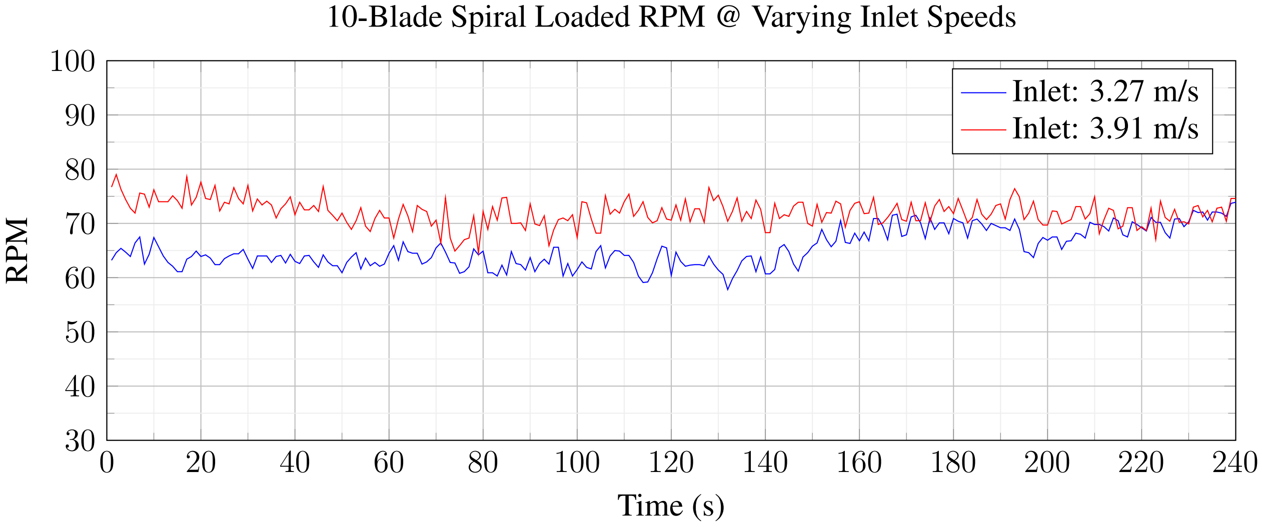

Figure 3.2: 10-Blade Spiral Loaded RPM vs Time [s] @ Speeds $\in V_{tun}$.

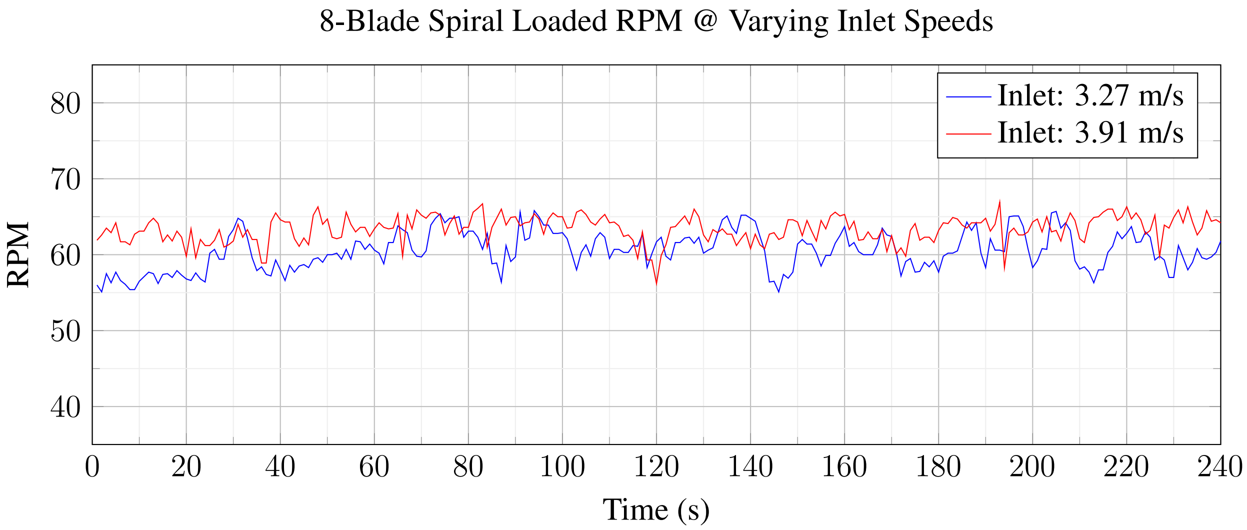

Figure 3.3: 8-Blade Spiral Loaded RPM vs Time [s] @ Speeds $\in V_{tun}$.

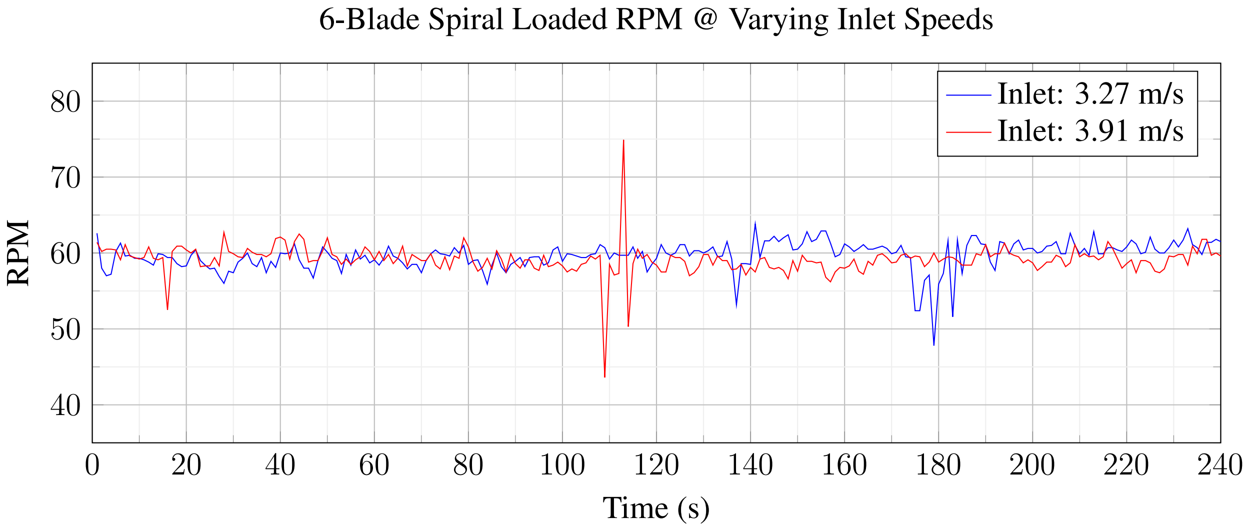

Figure 3.4: 6-Blade Spiral Loaded RPM vs Time [s] @ Speeds $\in V_{tun}$.

Note from the above graphics it can be inferred that as the number of blades is increased from 8 to 10, the loaded RPM of the Spiral configuration will increase at both inlet velocities. However, for configurations with 6-blades and potentially below, it seems this trend does not hold. This trend will further be verified in the following subsection. Additionally, it is worth noting that for both 8 and 10 blade configurations, the turbine exhibits higher RPM values at the faster inlet speed relative to the slower one; this indicates that the configuration may see a further increase in loaded RPM if tested at higher inlet velocities. This could indicate that it may have a higher optimal operational speed than tested.

3.1.1.2 Staggered

The following graphics display the measured loaded RPM for the Staggered configuration of the novel VAWT with (10, 8, 6) blades at the 2 varying fan-speeds $\in V_{tun}$.

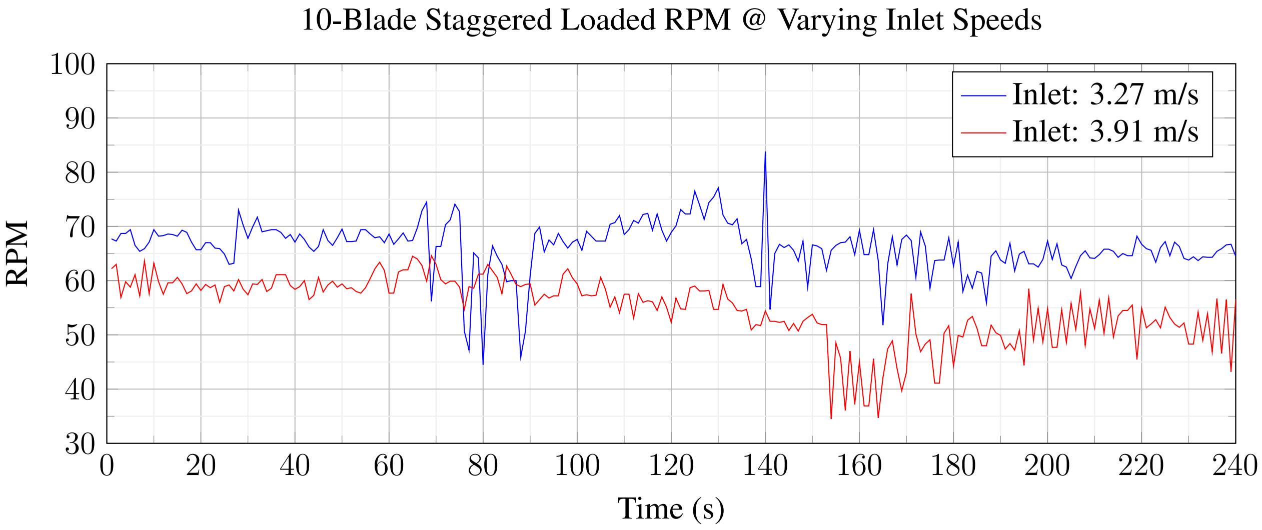

Figure 3.5: 10-Blade Staggered Loaded RPM vs Time [s] @ Speeds $\in V_{tun}$.

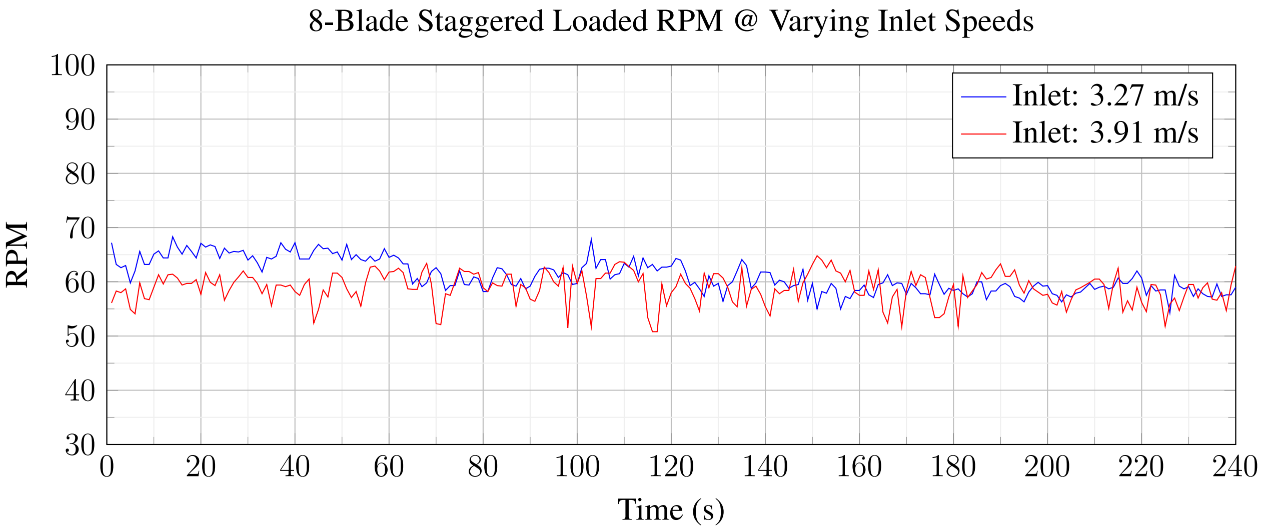

Figure 3.6: 8-Blade Staggered Loaded RPM vs Time [s] @ Speeds $\in V_{tun}$.

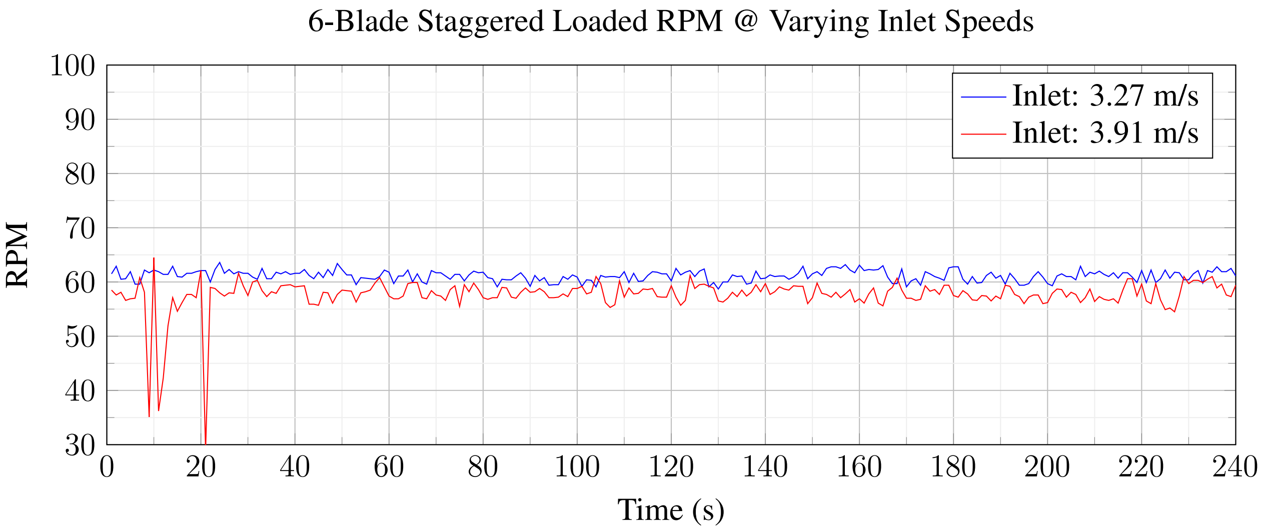

Figure 3.7: 6-Blade Staggered Loaded RPM vs Time [s] @ Speeds $\in V_{tun}$.

Each graphic represents the performance of the individual configurations for the 2 varying fan-speeds at the specified wind-tunnel distance. For the staggered configuration at all blade numbers, we see that it has a higher loaded RPM at the lower inlet velocity of $v = 3.27m/s$. This infers that the staggered configuration likely has a lower operational speed than the Spiral configuration; which is expected, as there is a greater period between applied drag forces on the blades in comparison to the Spiral configuration. Additionally, differences between the 6 and 8 blade configurations appears marginal graphically, which is also (partially) given the nature of the Staggered configuration:

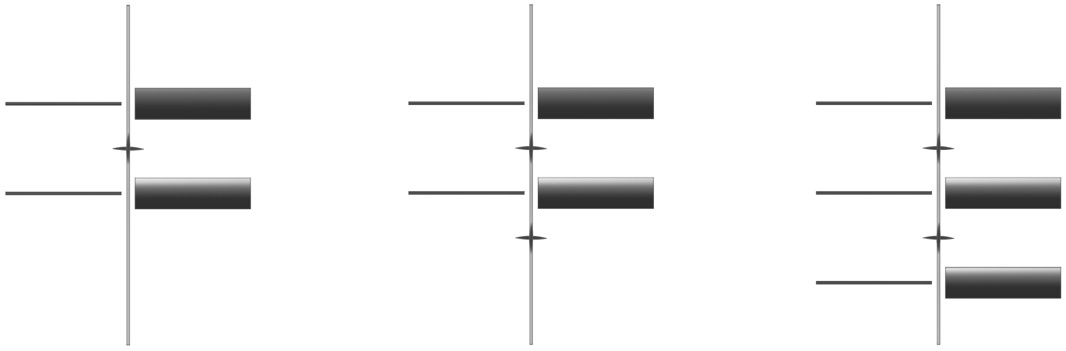

(a) 6-Blade (b) 8-Blade (c) 10-Blade

Figure 3.8: Staggered configuration frontal-view

The addition of a blade-pair from 6 blades adds a set of blades parallel to the wind-flow, as seen in the transition from Figure 3.8(a) → (b). Thus one portion of the blades rotation will remain unchanged, but the other adds an additional blade to the axis going into the page. This would have been thought to aid in stabilizing the motion of the configuration from Figure 3.8(a) → (b) → (c), however it seems to have had the opposite effect. Although 10-blade staggered configuration sees the highest loaded RPM values, it visibly appears to have the most fluctuations in its values; this could be a result of either the solid-fluid wake interaction or human error in measurement of values. Yet this trend seems to apply across all configurations with the 6-blade also being visibly the most consistent in its values in Figure 3.7.

3.1.1.3 Cross-Configuration Comparison

Here the 2 varying wind speeds for each blade number will be averaged to provide a clearer visual on the overall effect increasing the number of blades has on loaded RPM for the spiral and staggered configurations.

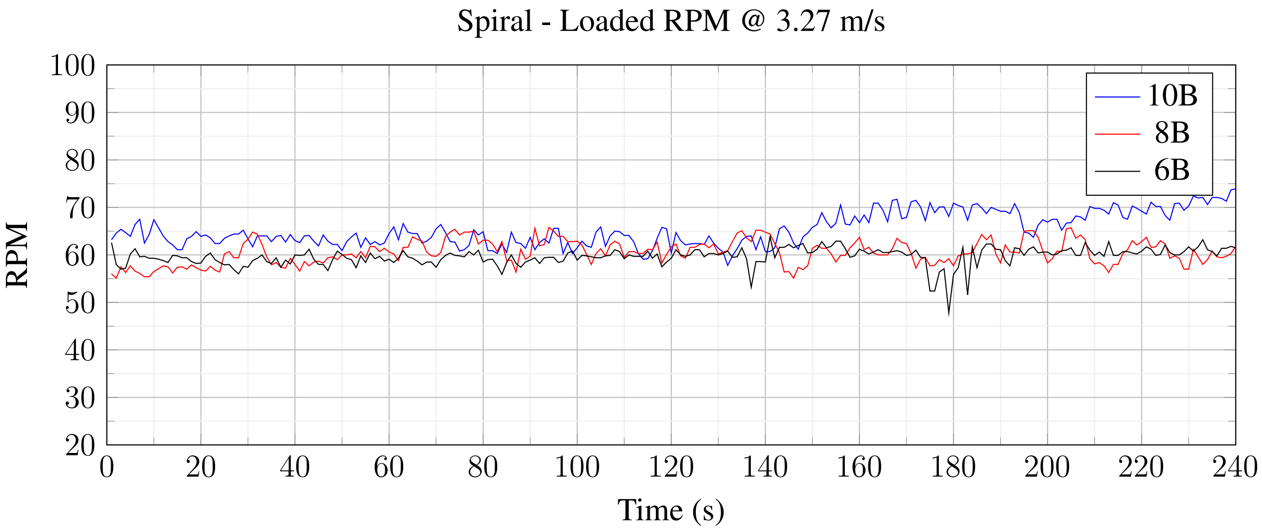

Figure 3.9: Spiral - Loaded RPM vs. Flow-Time [s] @ Inlet 3.27 m/s

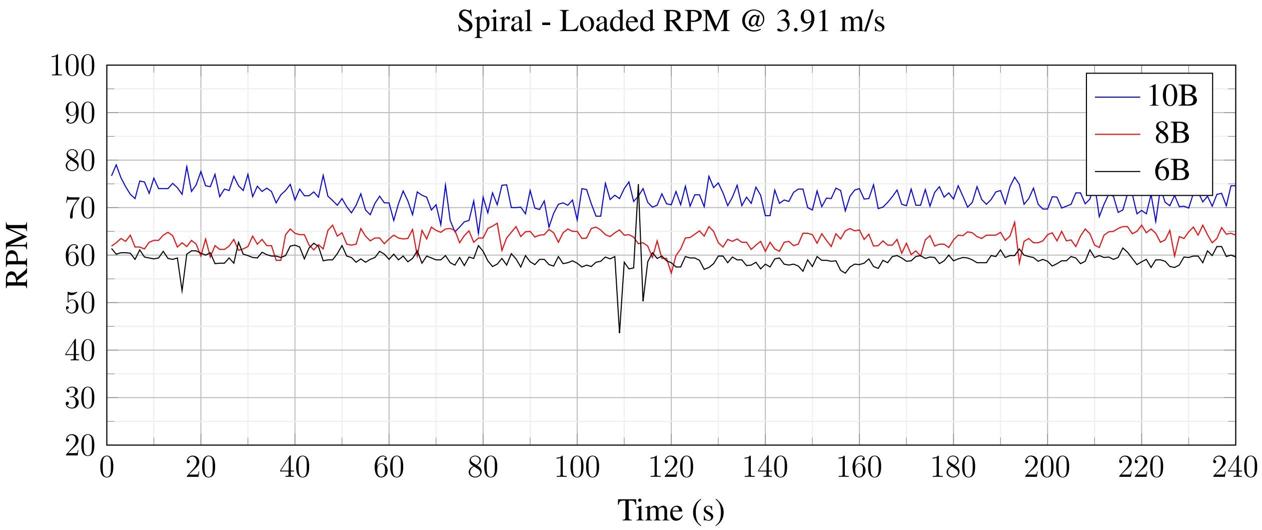

Figure 3.10: Spiral - Loaded RPM vs. Flow-Time [s] @ Inlet 3.91 m/s

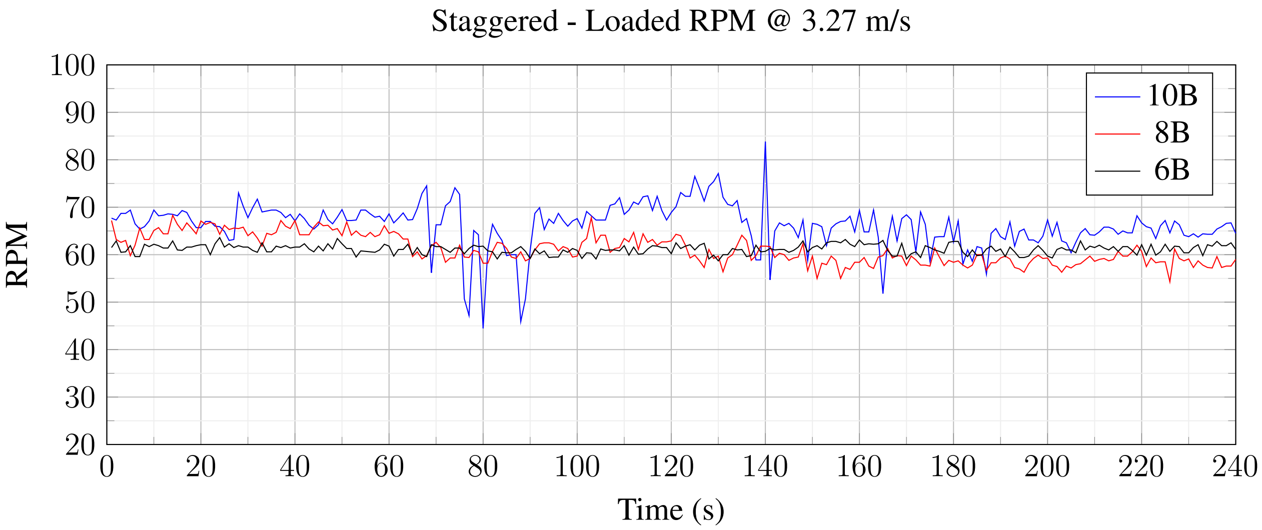

Figure 3.11: Staggered - Loaded RPM vs. Flow-Time [s] @ 3.27 m/s

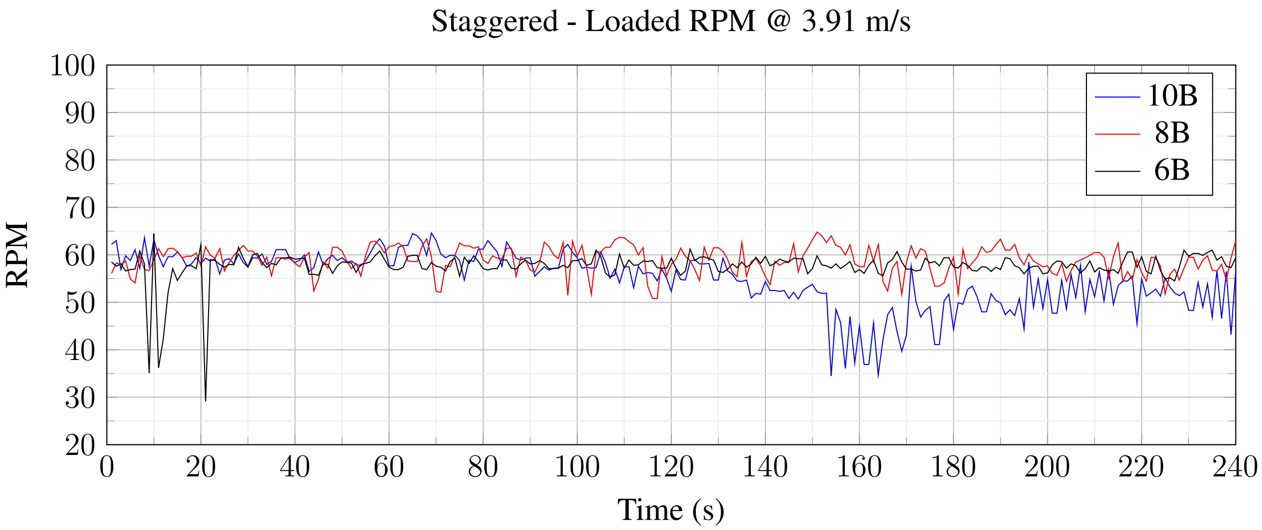

Figure 3.12: Spiral Configuration - Loaded RPM vs. Flow-Time [s] @ 3.91 m/s

The expected trend of Loaded RPM increasing as blade numbers increased remained relatively sound until observing the performance of the Staggered configuration @ $v = 3.91\ m/s$. Here it is noted that in fact past $t = 140s$, there is a stark reduction in the performance of the 10-blade configuration relative to the 8- and 6-blade, as shown in Figure 3.12.

The following figures depict variations in average and maximum loaded RPM over the chosen 240s time-interval for the Spiral and Staggered configurations at both inlet speeds $\in V_{tun}$.

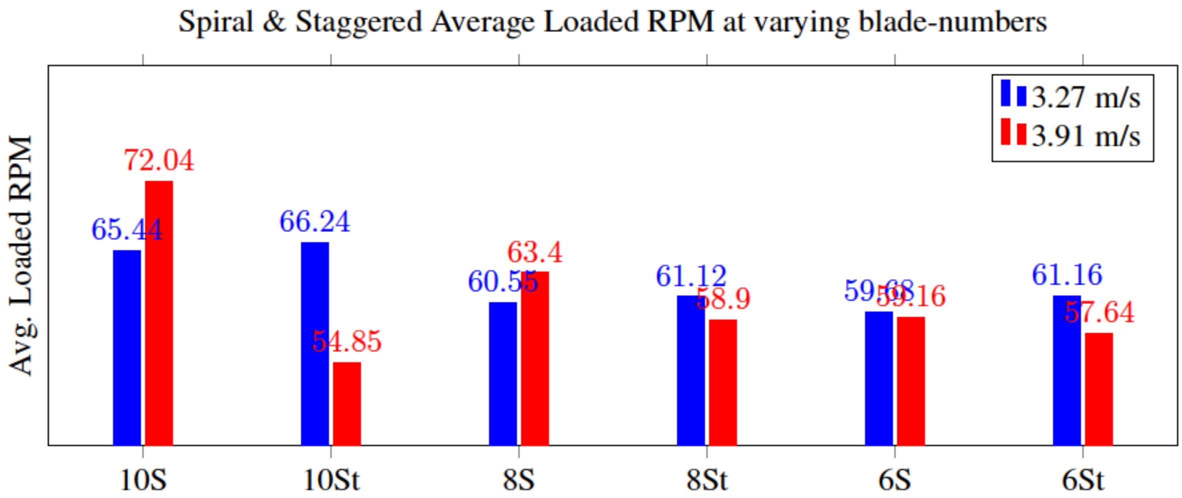

Figure 3.13: S-WIND Spiral & Staggered - Average Loaded RPM at varying blade-numbers and inlet velocities

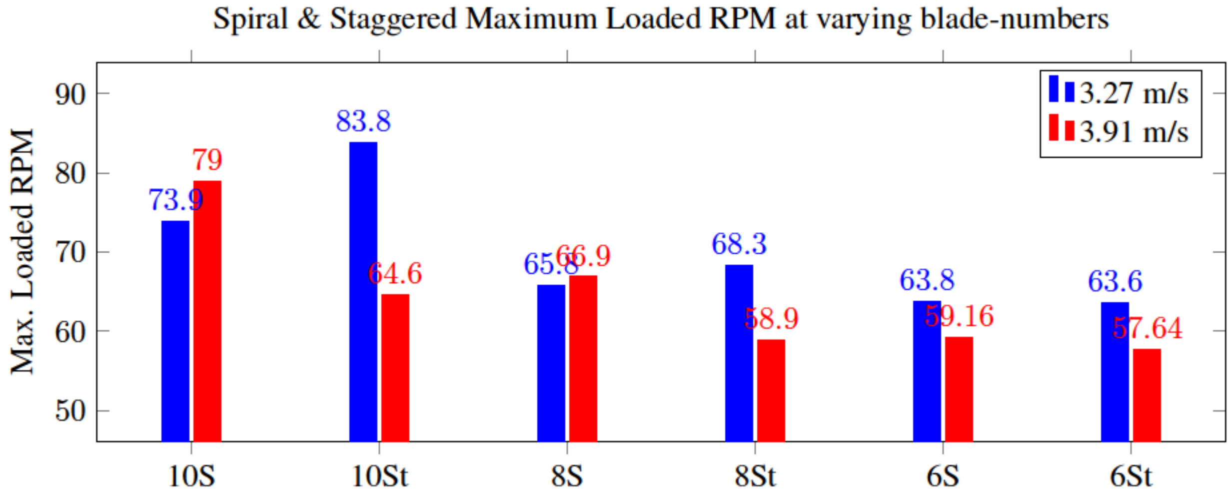

Figure 3.14: S-WIND Spiral & Staggered - Maximum Loaded RPM at varying blade-numbers and inlet velocities

3.1.2 Voltage (Power Errors)

Provided below are calculated values of Power for the selected experimental models. It is believed that a poorly-rated current on the provided turbine's motor is a potential reason for the substantially low values and low variance between calculated values. The provided motor has a maximally-rated current of $0.128A$ and from the method of recording never surpassed a value of $0.072A$, with an average current of $\sim 0.02A$. After recording the instantaneous values for both voltage and current across multiple configurations, the following formula for power was intended to be utilized:

$$P_{T_{exp.}} = V \times I \tag{3.1}$$

where V is the instantaneous voltage and I is the instantaneous current. However, the utilized formula for power provided graphics that did not make much physical sense. Voltages across all configurations did display separation across configurations as will be shown, however it is believed that errors either in measurements of the current, or in the maximal rating of the current negatively impacted results for power. Voltage graphs that are shown below are visuals of a condensed range of the total elapsed time, for better visual separation.

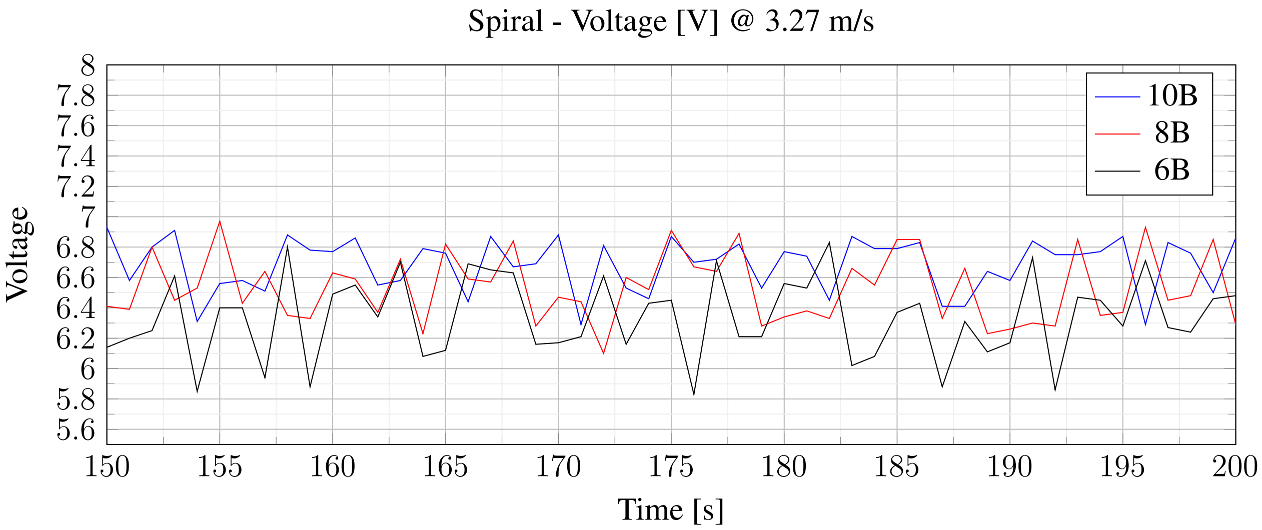

Figure 3.15: Spiral Configuration - Voltage vs. Flow-Time [s] @ 3.27 m/s

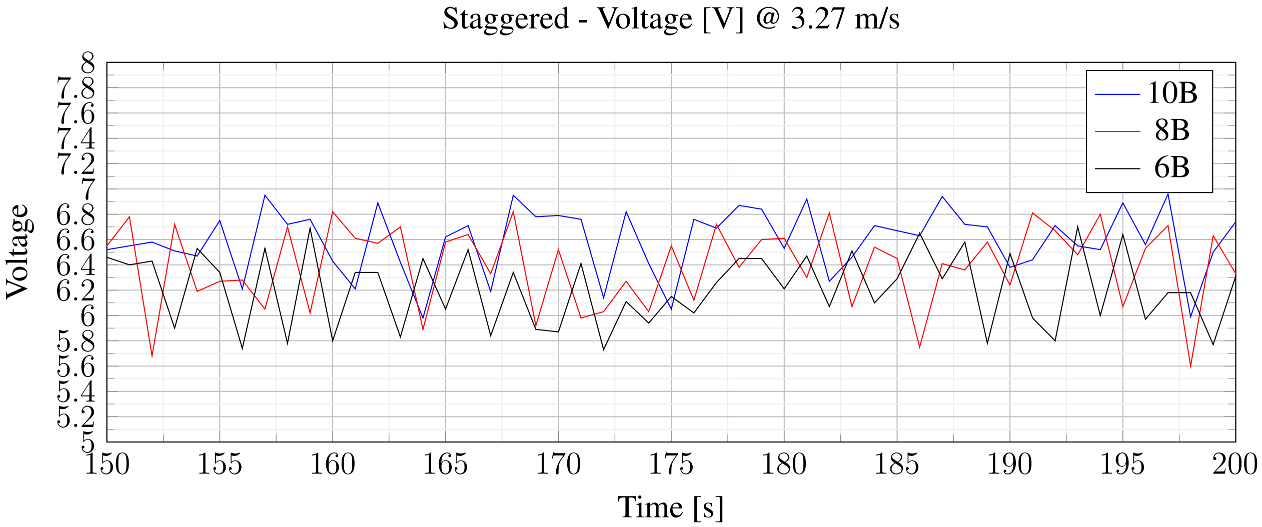

Figure 3.16: Staggered Configuration - Voltage vs. Flow-Time [s] @ 3.27 m/s

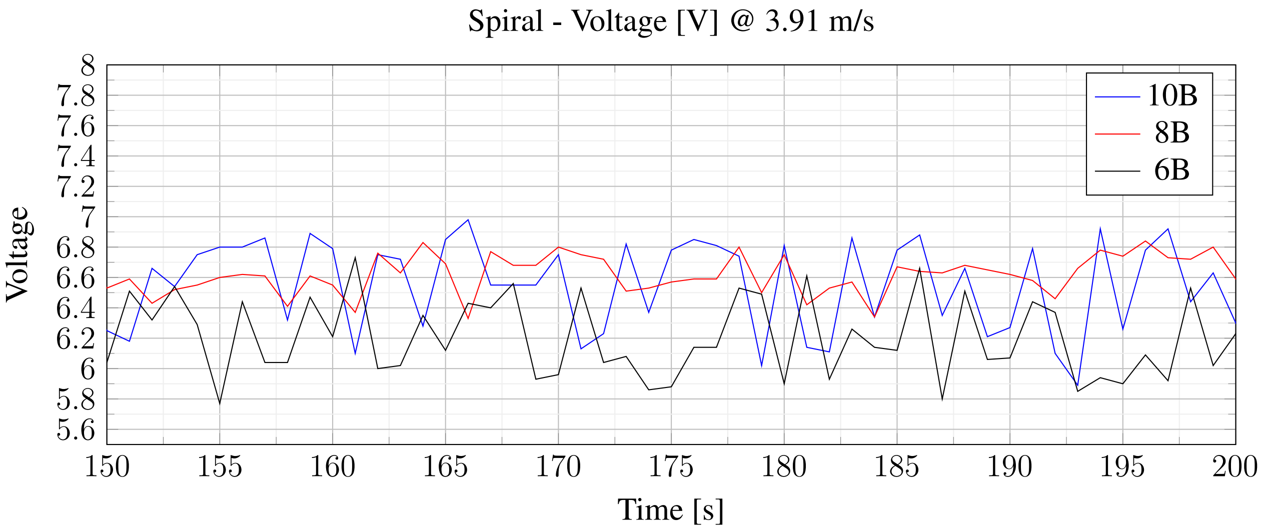

Figure 3.17: Spiral Configuration - Voltage vs. Flow-Time [s] @ 3.91 m/s

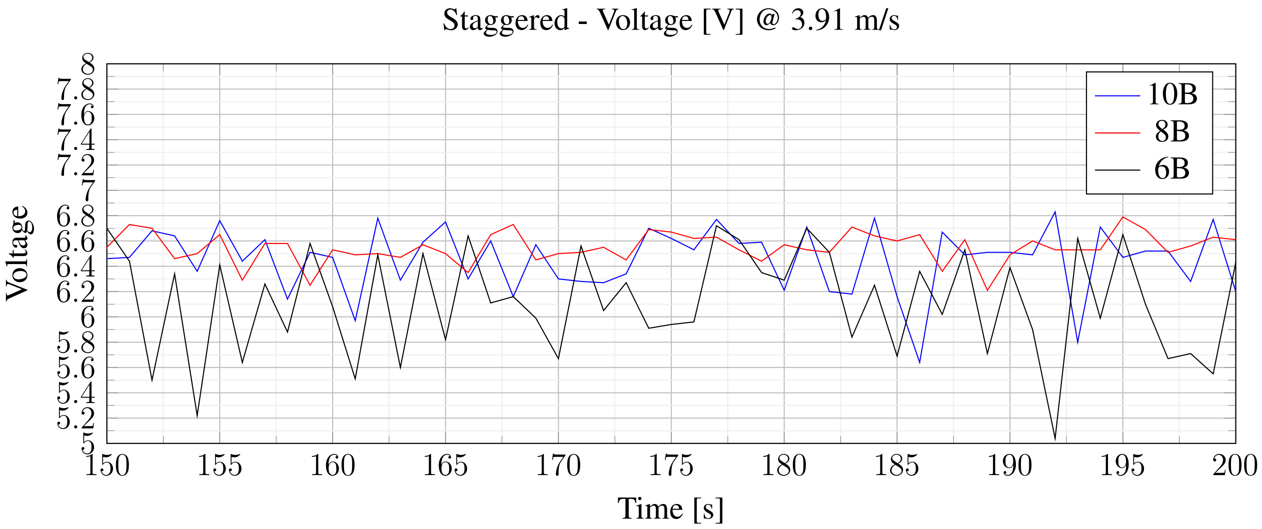

Figure 3.18: Staggered Configuration - Voltage vs. Flow-Time [s] @ 3.91 m/s

The graphics do demonstrate a clear rank-ordered separation between number of blades and peak voltage values across configurations, thus there is likely a correlation between the number of blades and peak power output even on the small-scale; however the tested number of blades do not represent any asymptotic trend as of yet. Experimental voltage is left as is and it is concluded that to generate more realistic values for power it is deemed necessary in future studies to ensure a motor is purchased with appropriate values for small-scale turbine power generation. Original anticipations of these findings were to utilize the values for a similarly-constructed CFD simulation to determine estimates at corresponding experimental TSRs and Power Efficiency (η) values. However, as a result of the significant amount of time spent accustoming to CFD software and working with single-blade pairs, the extend of these considerations were limited and can be followed-up on in future work.

3.2 Numerical Results

3.2.1 Single-Blade Pair Configurations

3.2.1.1 General Mesh Quality

To measure mesh quality, there are a number of mesh metrics that can be utilized for consideration. For the purposes of this research, the chosen metric of reference for mesh quality was 'Orthogonal Quality'. Since these simulations will all be 3-Dimensional, we will utilize most (if not all) of the allowed mesh elements since similar 3D VAWT-studies [1], [25], have utilized $\sim$ (10M, 5.5M) mesh elements respectively for 3D-analyses; similar studies in [**?**] demonstrate high mesh qualities despite element limitations, meaning there is consideration for improvement. Note that the applied mesh refinements bring considerable quality improvements and are utilized throughout several similar CFD studies for VAWTs ([17], [1]); yet according to the following Enhanced Mesh Orthogonal quality scale provided by [7], a fair percentage of mesh elements fall below the recommended values, specifically in regions surrounding the blade edges which indicate the source as the blade inflation layers.

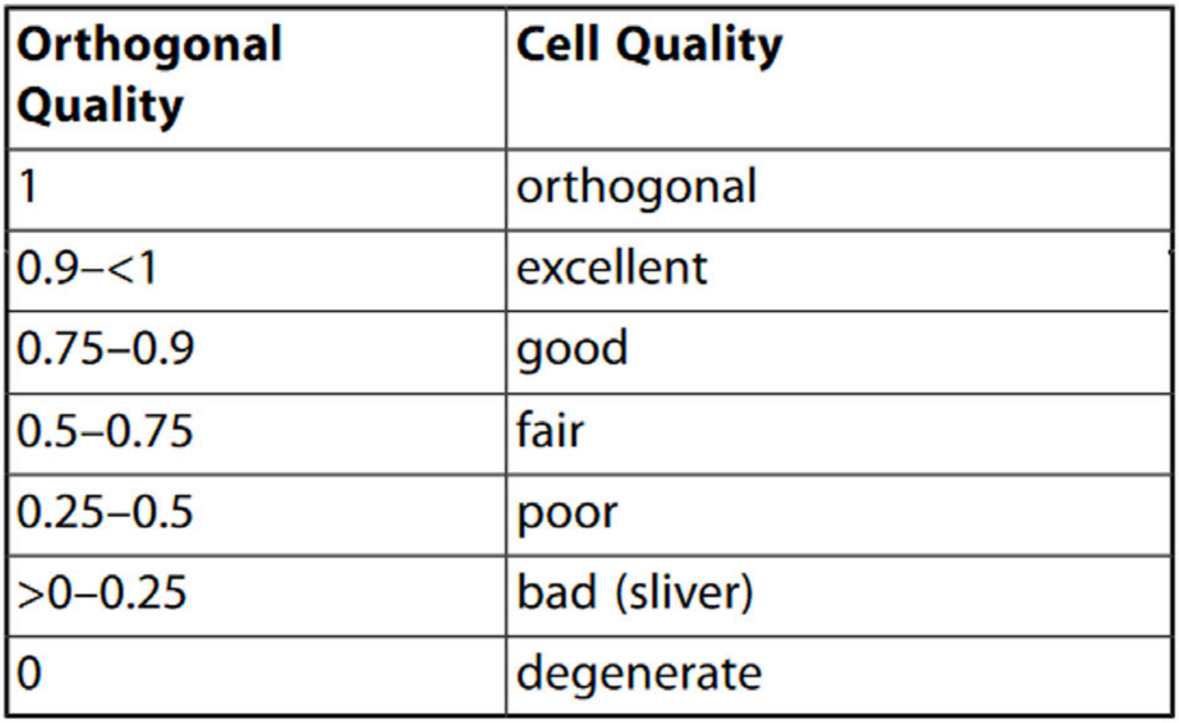

Orthogonal Quality	Cell Quality
1	orthogonal
0.9–<1	excellent
0.75–0.9	good
0.5–0.75	fair
0.25–0.5	poor
>0–0.25	bad (sliver)
0	degenerate

Figure 3.19: Mesh Orthogonal Quality range table [7]

Provided below are graphs displaying the orthogonal mesh qualities for all studied blade-profiles. A separate figure is provided after for the Savonius mesh quality, that demonstrates it also had a fair percentage of elements that fell below the 'recommended' values for mesh orthogonal quality. Thus further considerations should be made to ensure computational domain dimensions do not negatively affect solution values as performed in [23].

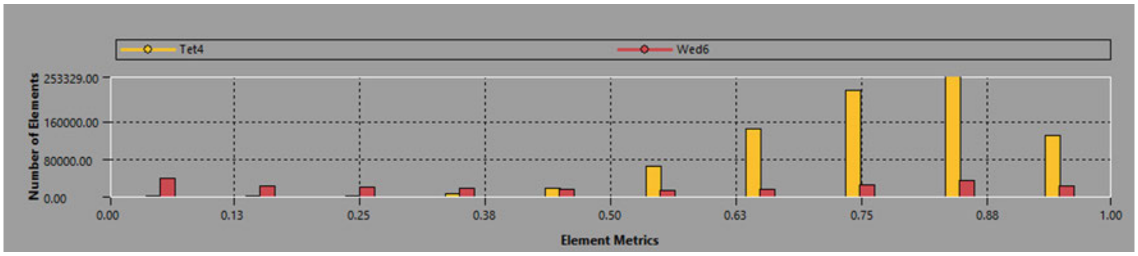

(a) G1 - Mesh Quality

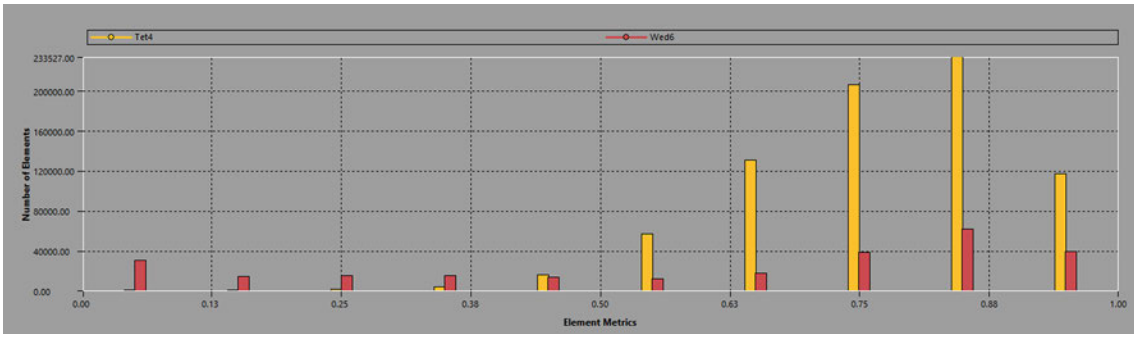

(b) G2 - Mesh Quality

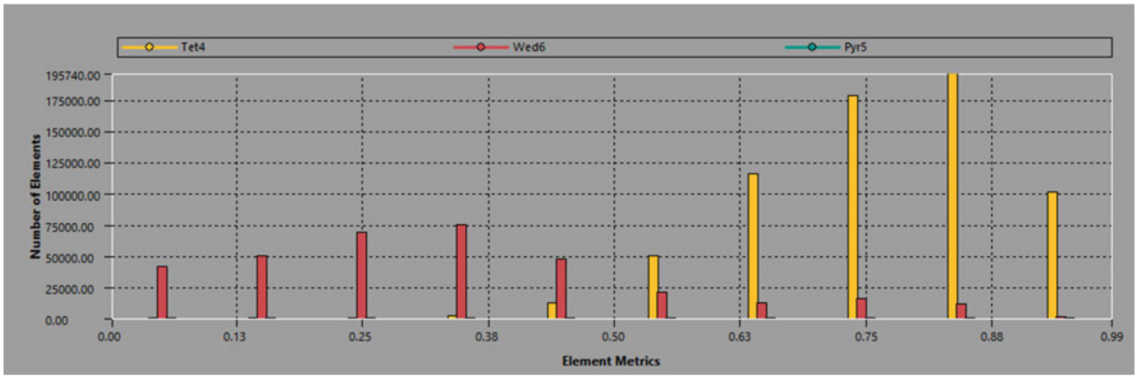

(c) G3 - Mesh Quality

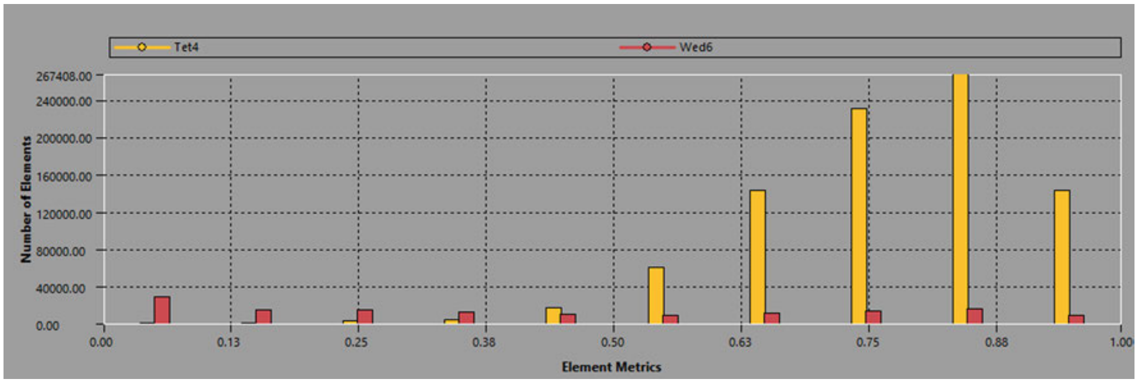

(d) G4 - Mesh Quality

Figure 3.20: Overall mesh quality for all novel blade-profiles

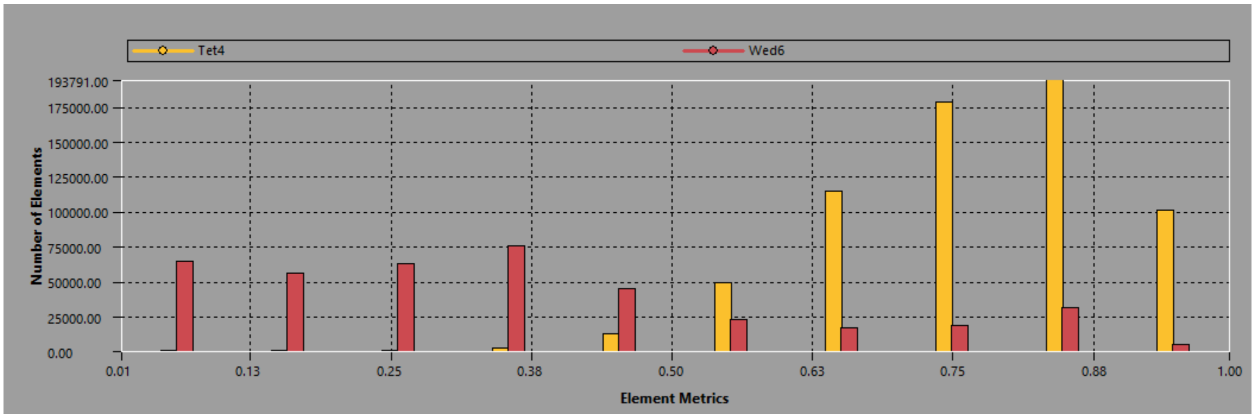

Figure 3.21: Overall mesh quality for Savonius geometry

In the above figures, the varying colors in the histograms are representative of varying mesh-shapes: red being Prism (wedge) mesh elements and yellow being Tetrahedral mesh elements. The prism mesh elements are the result of the added layers of inflation. The X-axis ranges from [0,1], which is of course equivalent to the provided scale in Figure 3.19, and is utilized to reference cell-mesh quality. The Y-axis of the histogram represents the number of elements falling within these orthogonal quality ranges. These figures depict that future improvements must be made to the inflation layers, else they should be removed to improve mesh quality.

3.2.1.2 Time-step Optimization Study

In transient analyses, the selection of an optimal time-step (T-s) size that accurately captures the dynamic behavior of the model, while minimizing computational time is essential; This is especially true when a large-number of simulations need to be run to test the effects of altered parameters. 5 time-steps were selected:

$$\Delta T = (0.1s,\ 0.05s,\ 0.01s,\ 0.005s,\ 0.001s) \tag{3.2}$$

The initially provided blade design (G1) was the selected blade-profile for the determination of an optimal time-step. Sliding Mesh simulations are run for each time-step sizing, and comparisons of performance quantities are analyzed.

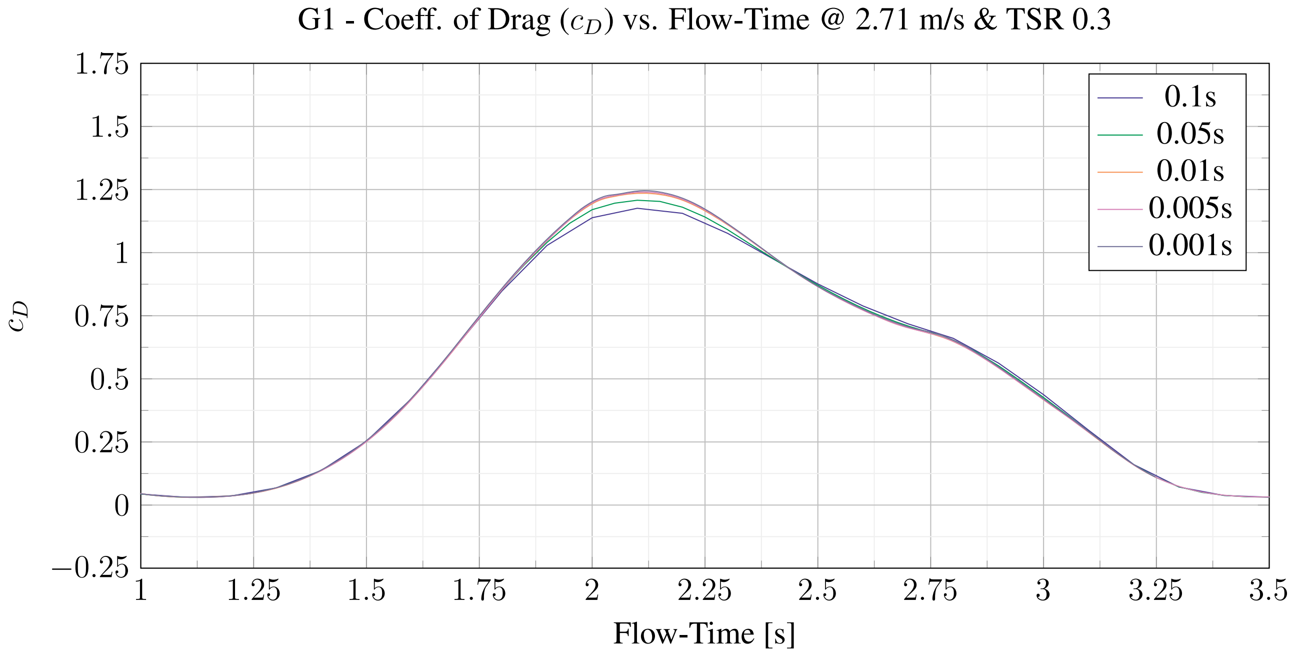

Figure 3.22: Time-step Analysis - C_D as a function of flow-time [s]

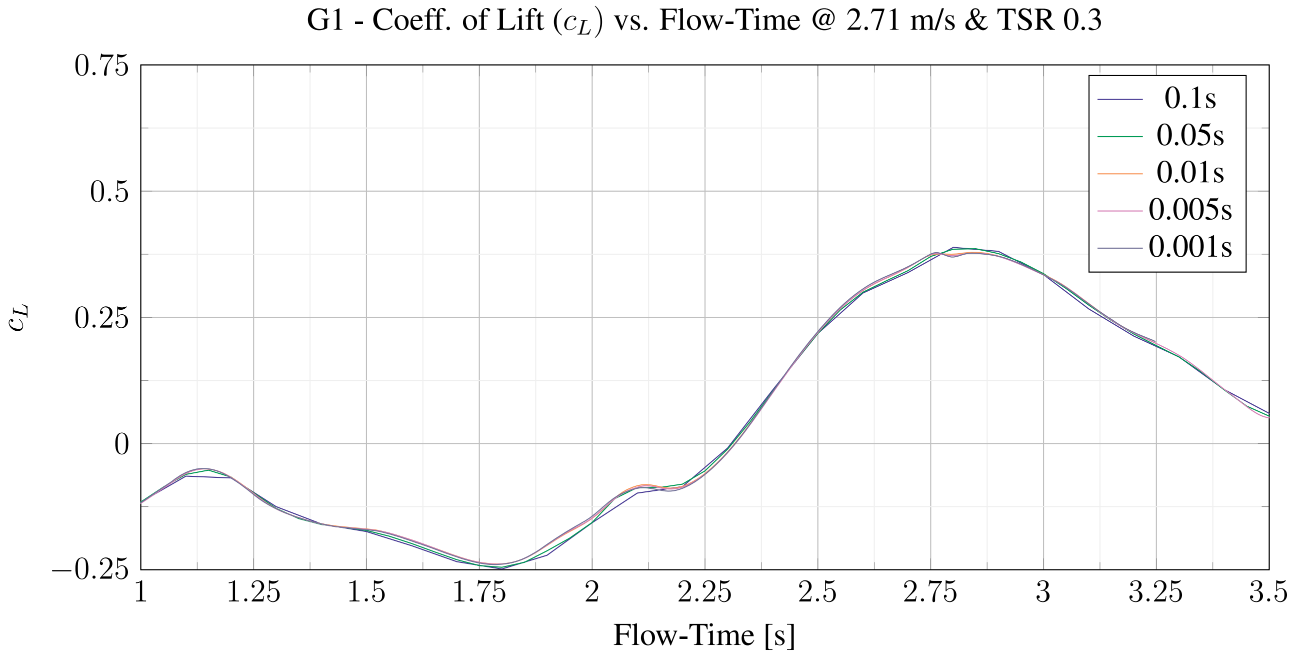

Figure 3.23: Time-step Analysis - C_L as a function of flow-time [s]

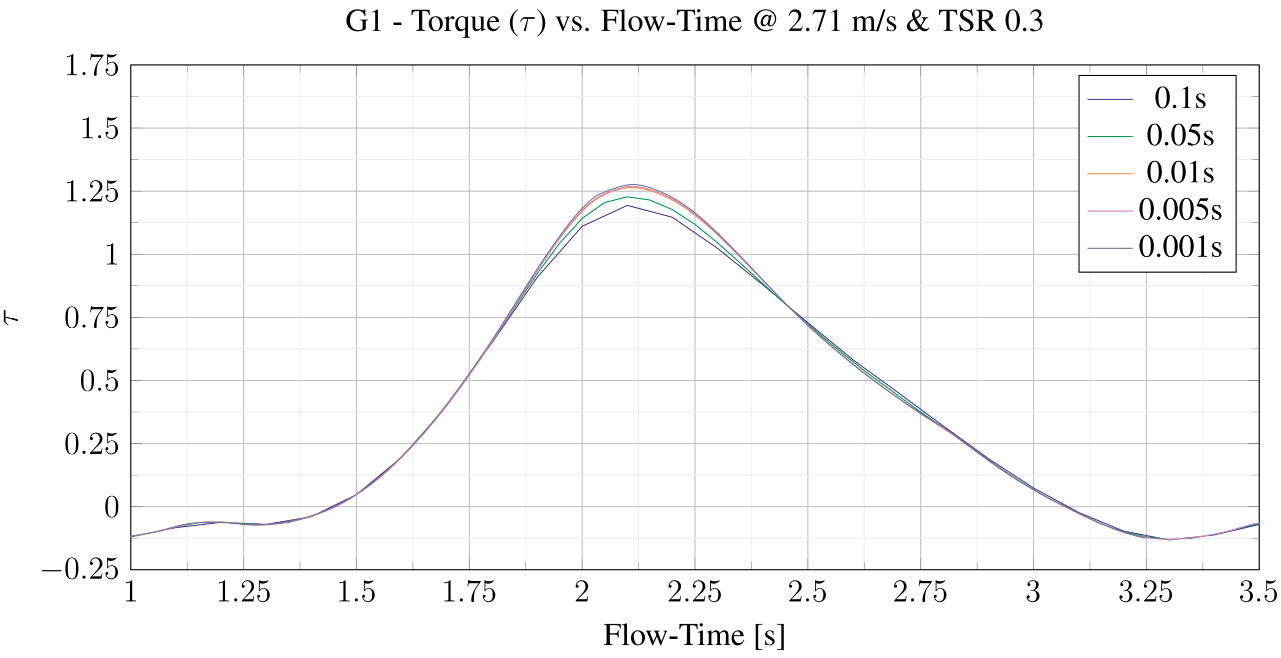

Figure 3.24: Time-step Analysis - τ as a function of flow-time [s]

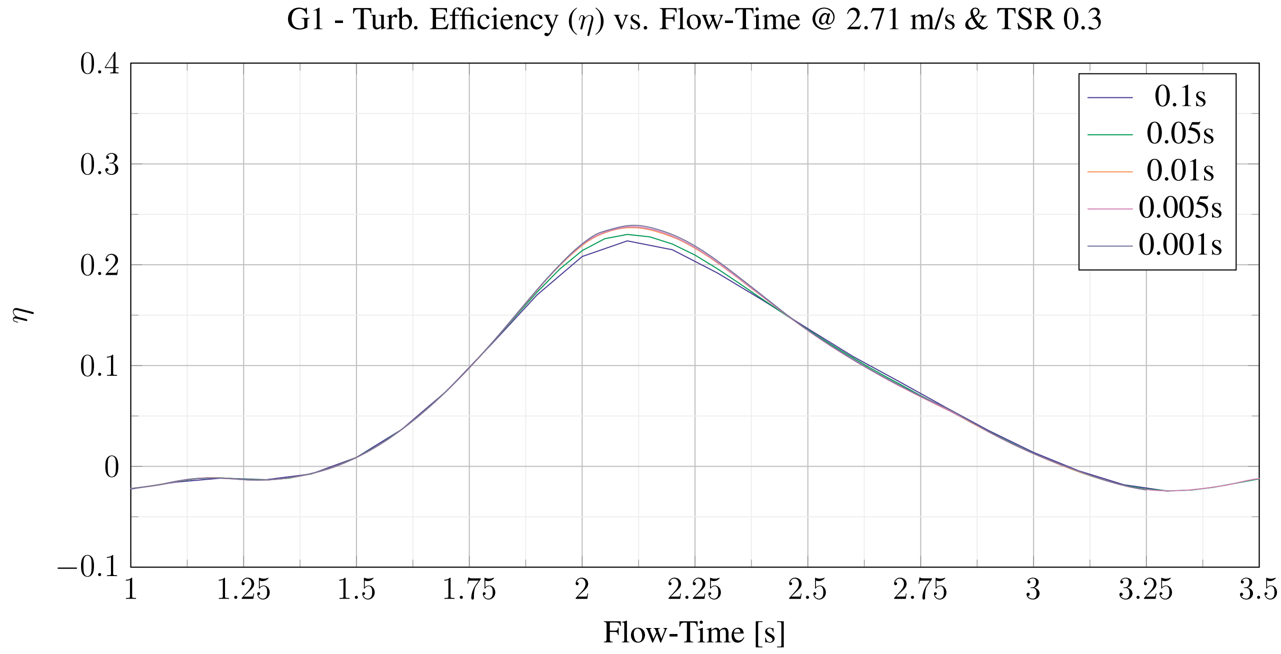

Figure 3.25: Time-step Analysis - η as a function of flow-time [s]

(T-s) size (s)	η_{max}	η_{avg}	$\eta_{0.001_{max}}$ % Err.	$\eta_{0.001_{avg}}$ % Err.	# (T-S)	# Iter.
0.1	0.224	0.072	10.86%	6.497%	33	705
0.05	0.230	0.077	4.721%	3.832%	65	3700
0.01	0.237	0.080	1.225%	0.991%	325	7115
0.005	0.238	0.081	0.811%	0.648%	650	11050
0.001	0.239	0.081	-	-	3250	17598

Table 3.1: Time-step sizing simulation details over one full revolution

The provided graphics display reductions in the fluctuation of instantaneous values for quantities of interest as time-step sizing is reduced. However, running simulations with the finer time-step sizes leads to dramatic increases in computational runtime. For context, running 17598 iterations for $\Delta t = 0.001s$ took well over 8 hours; that is just to run one-revolution. Thus the selected time-step size for all further transient simulations is established as $\Delta t = 0.05s$. We observe % errors for $\Delta t = 0.05s$ relative to the finest time-step sizing to be under 5%. If a smaller number of simulations were to be run in future analyses (≤ 10), $\Delta t = 0.01s$ is seemingly a more appropriate selection for transient time-step sizing, as the relative % error for η is (≤ 2); This would additionally align with the selected time-step sizing utilized in [1].

3.2.1.3 Aerodynamic Performance Analysis

Improving the capabilities of a model's blade-profile is an important consideration in its optimization process. Thus we consider the 4 blade-profiles referenced in Figure 2.10, duplicate them to be single blade-pairs (smaller-scale turbines; as described in the Methodology), and simulate their performances at varying TSRs of the selected inlet, $v = 2.71\ m/s$. Again, the main metric of interest is power efficiency, and thus the moving average of the models' efficiencies over 3 full turbine revolutions will be presented both as functions of λ and as functions of ω. It is useful to also plot differences in other quantities, such as c_D, c_L, τ; these can be plotted as instantaneous functions of flow-time. Additionally, a Savonius rotor with an equivalent frontal facing area of $1ft^2 \equiv 0.092903m^2$ will also be tested to serve as a comparative analysis. Instantaneous flow-time figures for the specified report definitions are shown below:

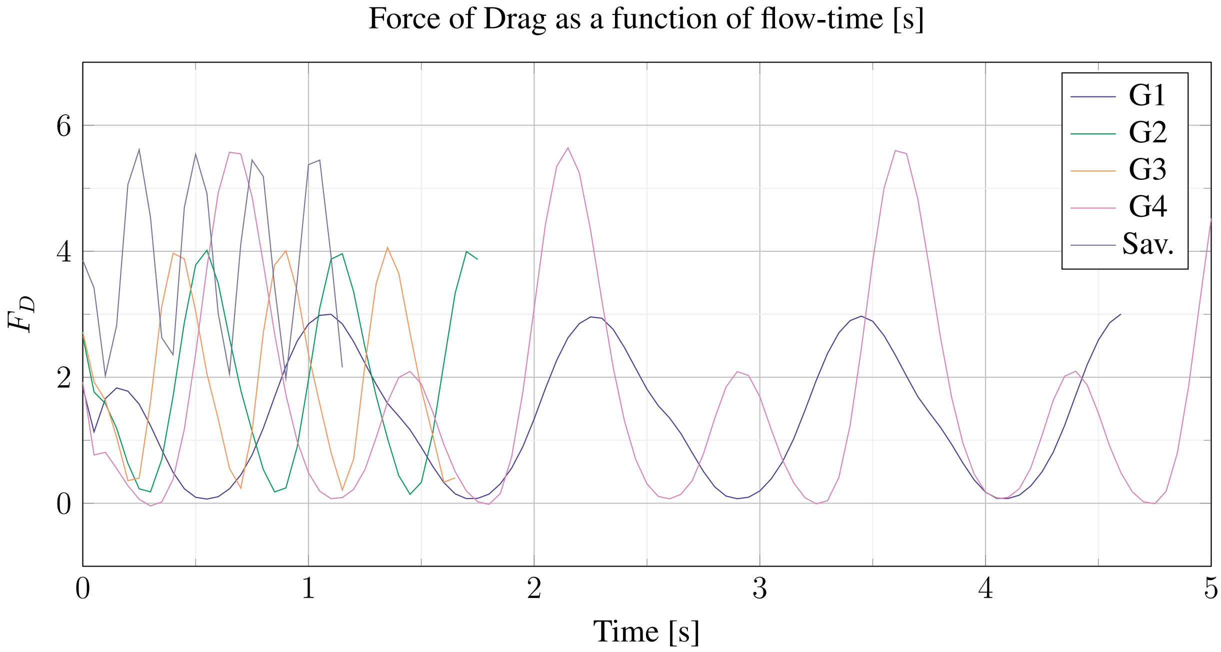

Figure 3.26: Force of Drag across blade-profiles as a function of flow-time [s]

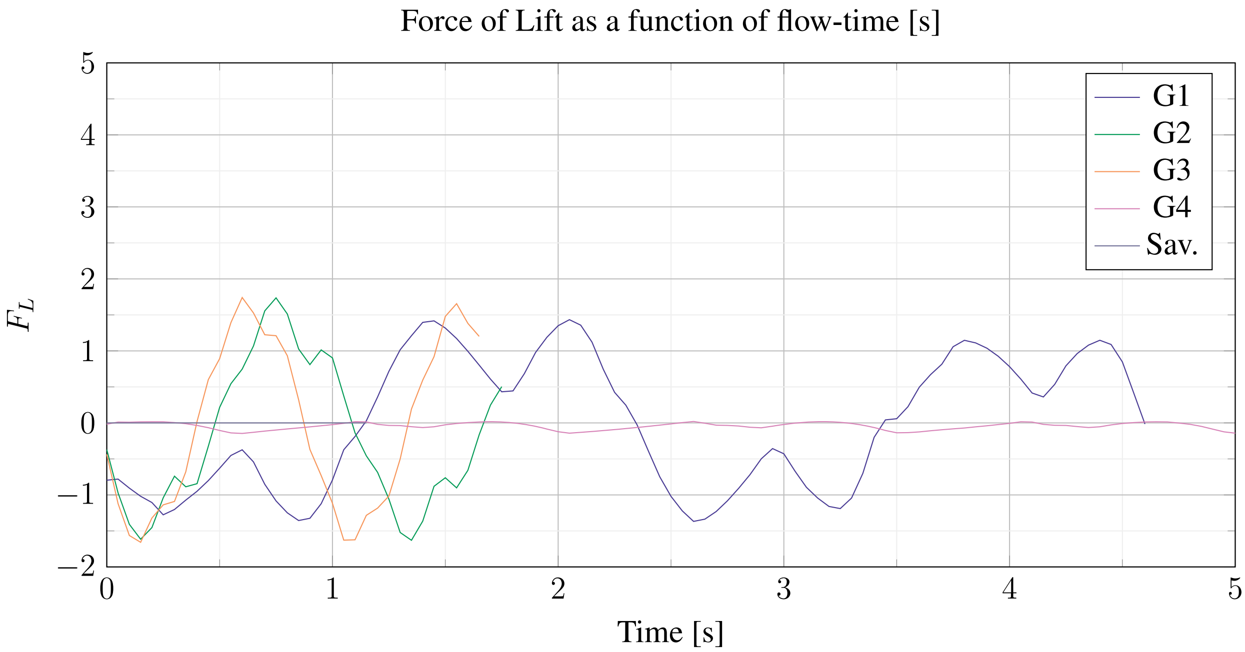

Figure 3.27: Force of Lift across blade-profiles as a function of flow-time [s]

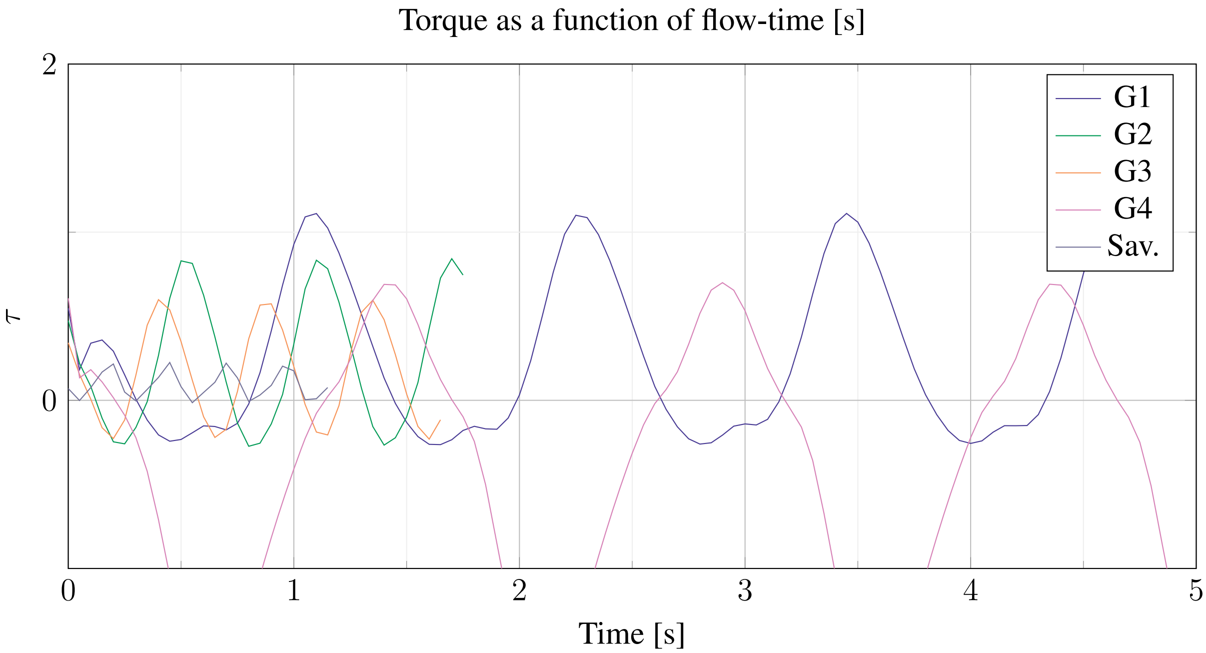

Figure 3.28: Torque across blade-profiles as a function of flow-time [s]

Note that blade-profile (d) (G4) exhibits large negative torque values relative to the other configurations, this is because there is no flap-region motion prescribed on G4, since its geometry is asymmetric; meaning the negative torque values are not physically significant for analysis. We note the highest values of torque for blade-profile (a) (G1) which is expected, considering it has the longest moment length. Blade profile (b) (G2) sees the second highest-values for torque, higher than the recorded values for blade-profile (d) (G4). The Savonius configuration sees the lowest net-torque values, which is partially expected as the negative torque from the returning blade has negative effects on the positive torque from the advancing blade.

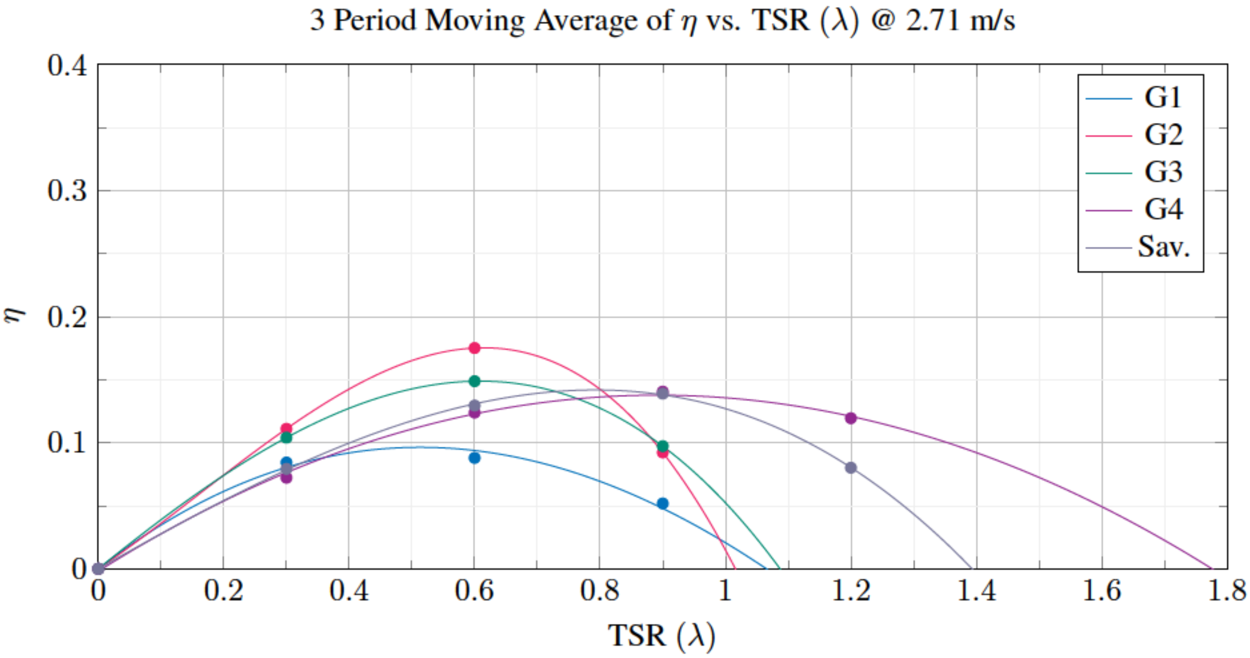

Figure 3.29: 3-Period Moving Average of η across blade-profiles as a function of λ

Note that $\lambda > 1$ for the drag-based VAWT is not practical for standalone systems without blockage or pitch mechanisms; meaning these representations are solely to demonstrate the power-curves and subsequent reduction in the power-curves at these non-physically attainable conditions. However, the addition of the flap region does provide additional lift force, and may raise operational TSR of said model. It is beneficial to additionally represent the above figure as a function of ω to provide a clearer visual on estimated ranges of 'optimal' operating speeds for the blade-profiles.

Geometry: TSR (λ)	G1	G2	G3	G4
0.3	0.0843	0.1111	0.1041	0.0723
0.6	0.0888	0.1752	0.1489	0.1240
0.9	0.0518	0.0923	0.0973	0.1406
1.2	-0.0508	-	-	0.1195

Table 3.2: 3-Period Moving Average of η vs. TSR (λ) @ 2.71 m/s

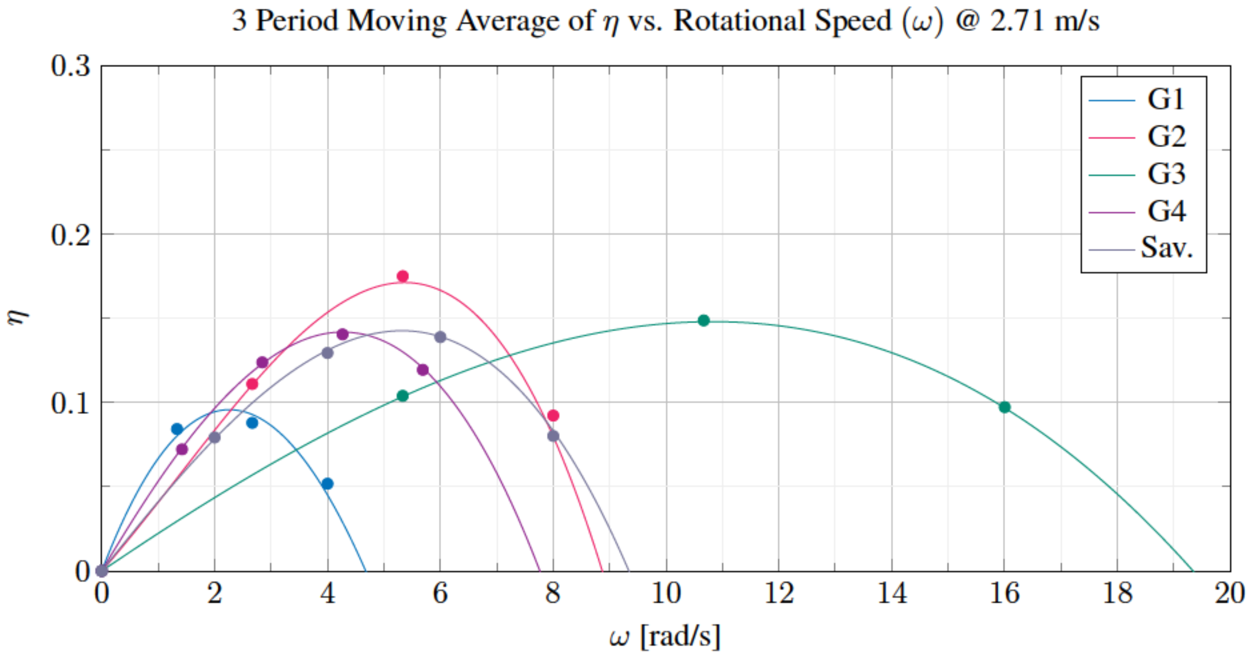

Figure 3.30: 3-Period Moving Average of η across blade-profiles as a function of ω

It is noted that the originally proposed design, blade-profile (a) i.e. (G1) is considered the least efficient of all configurations, due to its low operational speed. Blade-profile (b) i.e. (G2) achieves the highest 3-period moving average for $\eta = 0.1752$ @ $\lambda = 0.6$ due to it is high-torque and high-operational speed, assuming it is capable of reaching said ω. The found value for η for (G2) exceeds that of the tested Savonius configuration, $\eta_{sav} = 0.1390$. Observe that blade-profile (c) i.e. (G3) in

Figure 3.19 has a considerably higher operating rotational speed (ω) range; however the practicality of this model's performance at these speeds is low, as it is considerably more difficult to alter blade pitch as blade height increases on full-turbine configurations due to spacing issues between blade-pairs. Increases in blade height also result in a larger produced torque about the blades' axes, which can add considerable mechanical stress on any proposed blade pitch mechanism. Blade-profile (d) (G4) exhibits maximum average efficiency values nearly equivalent to that of the Savonius, which is within reasoning since there was no prescribed flap-motion for (G4), meaning their is no rotation of the blades about their own axes. This implies the motion for (G4) is purely reliant on the drag force, and thus no lift is generated; Meaning that it is then expected for the behavior of this profile to have similar results to that of a typical drag-based Savonius configuration. This is also likely why we see a higher operational $\lambda = 0.9$, equal to that of the Savonius, for (G4).

3.2.1.4 Contours

These below images depict contours of both velocity and pressure for each of the proposed blade-profiles at an inlet velocity of $v = 2.71\ m/s$, and at each of the blade-profile's optimal-(λ) as extrapolated in the Aerodynamic Performance Analysis. Both velocity and pressure contours are depicted as top-down views of the blade-pairs, with the wind flowing from left to right. The progression of the images in each figure depicts the varying behavior at different AoA for each blade-profile. These contours are the result of the utilization of tetrahedral and prism mesh elements as composed in the standalone Fluent ®Mesh module as described in Chapter 2.

Velocity Below are figures representing differing velocity contours for geometries at their optimal values for λ. The provided images are shown from the a top-down view, with the inlet on the left and outlet on the right. Each blade profile has four images corresponding to different points of contact on the DW and LW portion of their revolution. For blade profiles (b), (c), and the Savonius, discontinuity regions are seen surrounding the flap region, additionally for all velocity contours a higher than expected maximum magnitude was seen. Improvements in mesh quality and re-investigation of the interface regions will likely remove these issues.

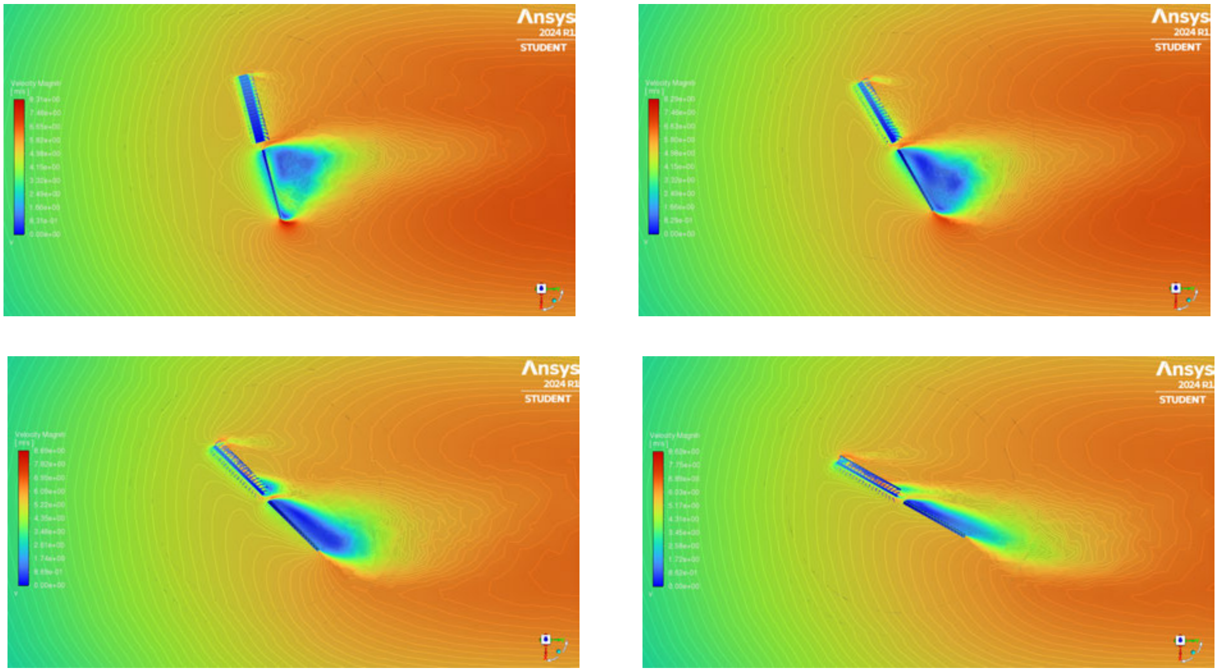

Figure 3.31: Blade-profile (a) (G1) velocity contours @ $v = 2.71\ m/s$ & $\lambda = 0.6$

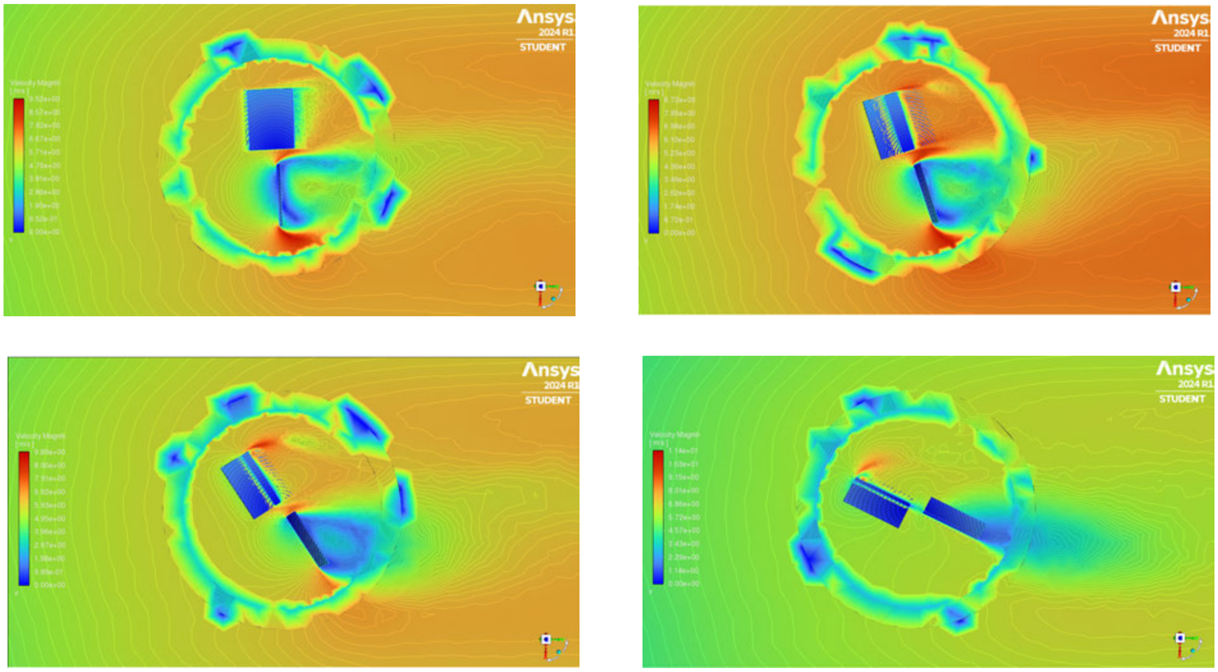

Figure 3.32: Blade-profile (b) (G2) velocity contours @ $v = 2.71\ m/s$ & $\lambda = 0.6$

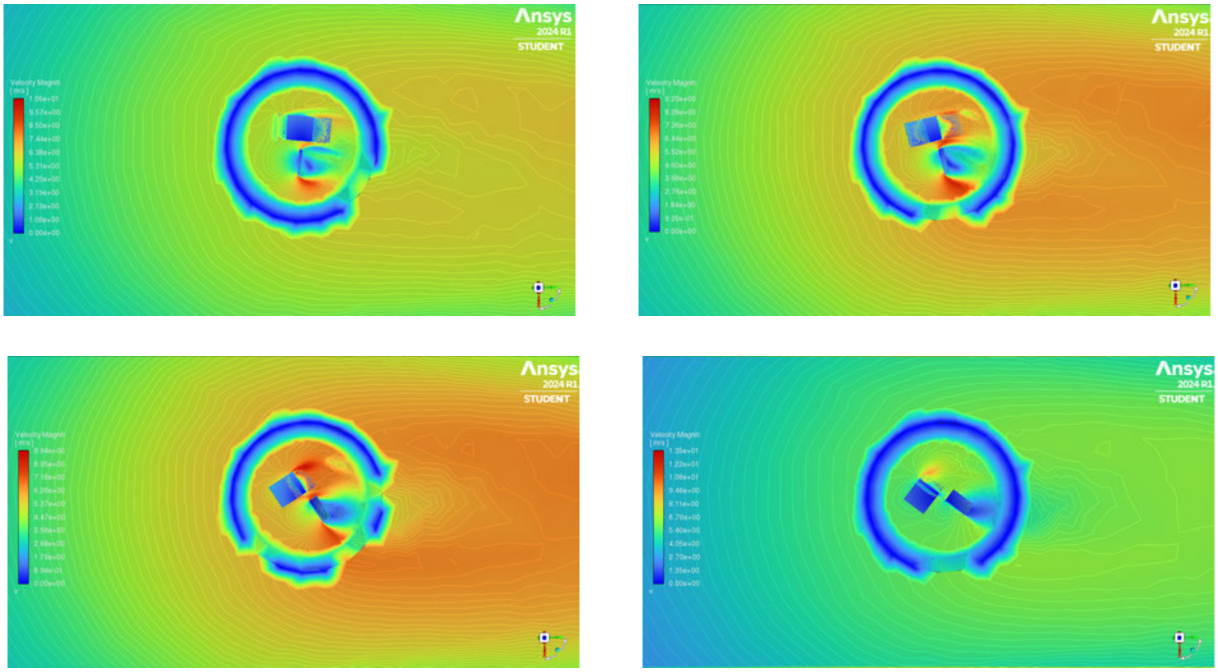

Figure 3.33: Blade-profile (c) (G3) velocity contours @ $v = 2.71\ m/s$ & $\lambda = 0.6$

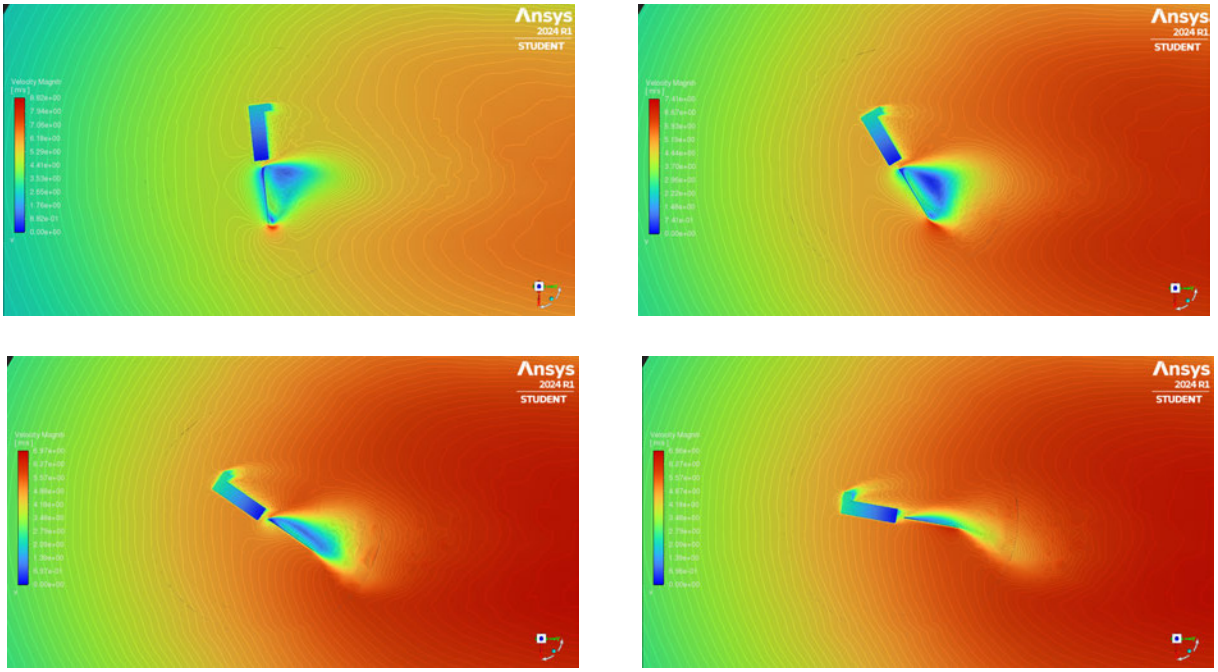

Figure 3.34: Blade-profile (d) (G4) velocity contours @ $v = 2.71\ m/s$ & $\lambda = 0.9$

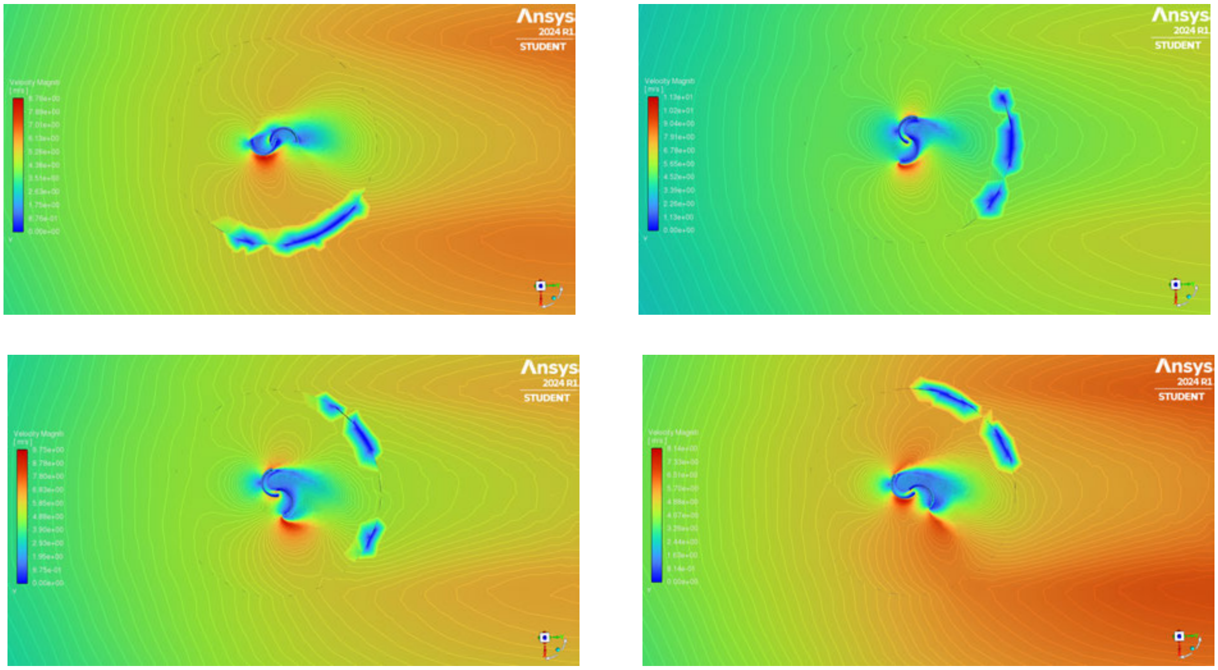

Figure 3.35: Savonius velocity contours @ $v = 2.71\ m/s$ & $\lambda = 0.9$

Pressure Below are figures representing differing pressure contours for geometries at their optimal values for λ. The provided images are shown from the a top-down view, with the inlet on the left and outlet on the right. Each blade profile has four images corresponding to different points of contact on the DW and LW portion of their revolution.

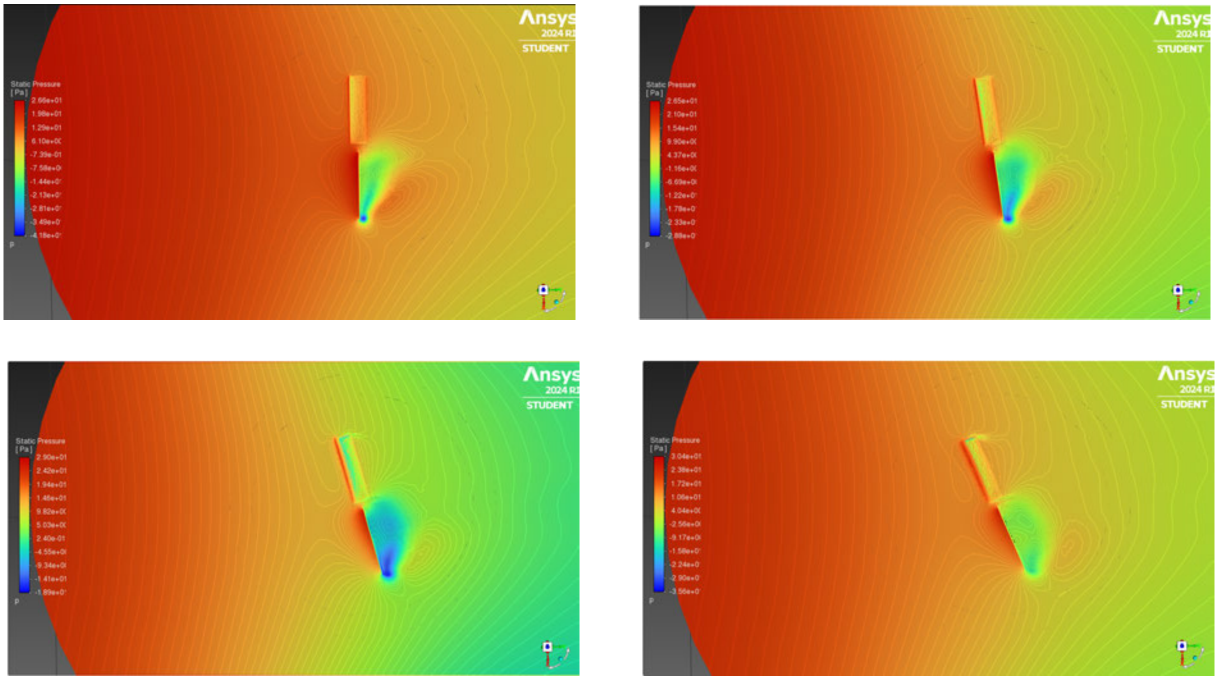

Figure 3.36: Blade-profile (a) (G1) pressure contours @ $v = 2.71\ m/s$ & $\lambda = 0.6$

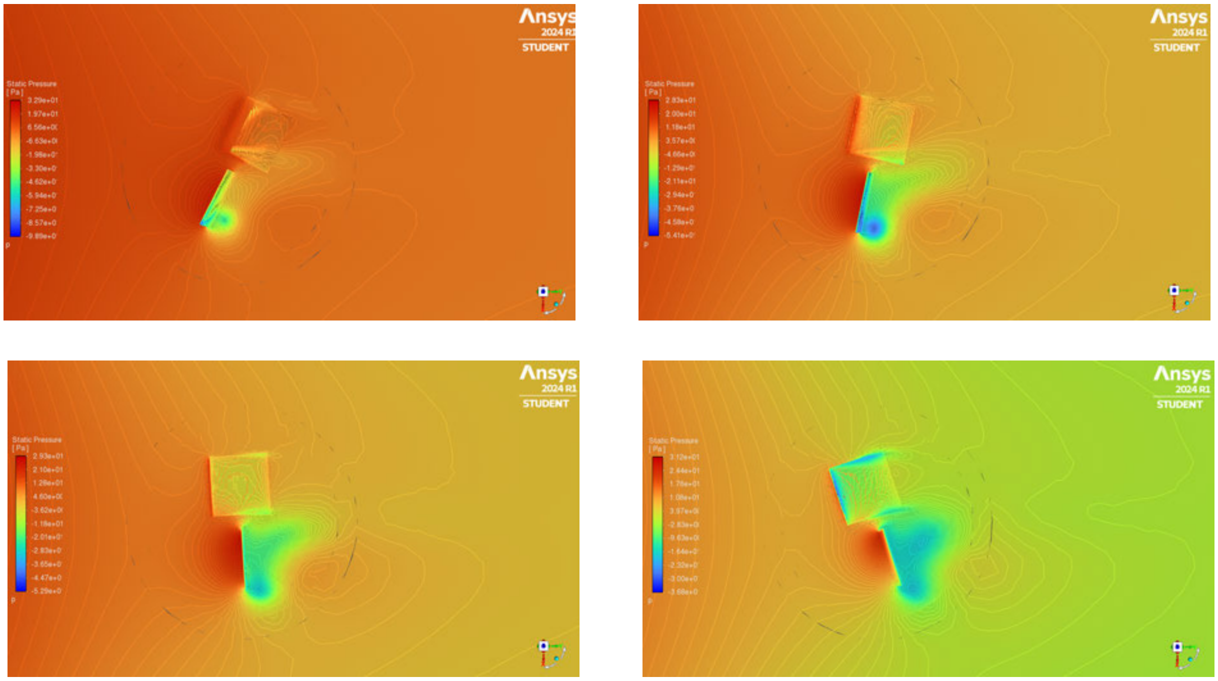

Figure 3.37: Blade-profile (b) (G2) pressure contours @ $v = 2.71\ m/s$ & $\lambda = 0.6$

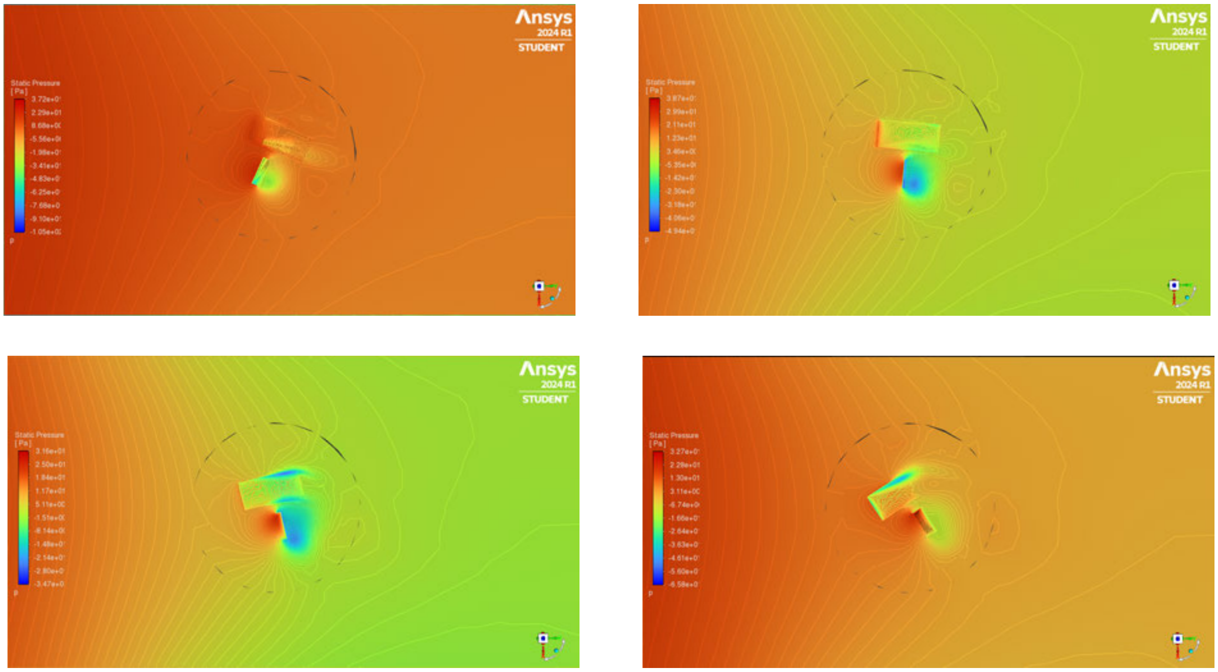

Figure 3.38: Blade-profile (c) (G3) pressure contours @ $v = 2.71\ m/s$ & $\lambda = 0.6$

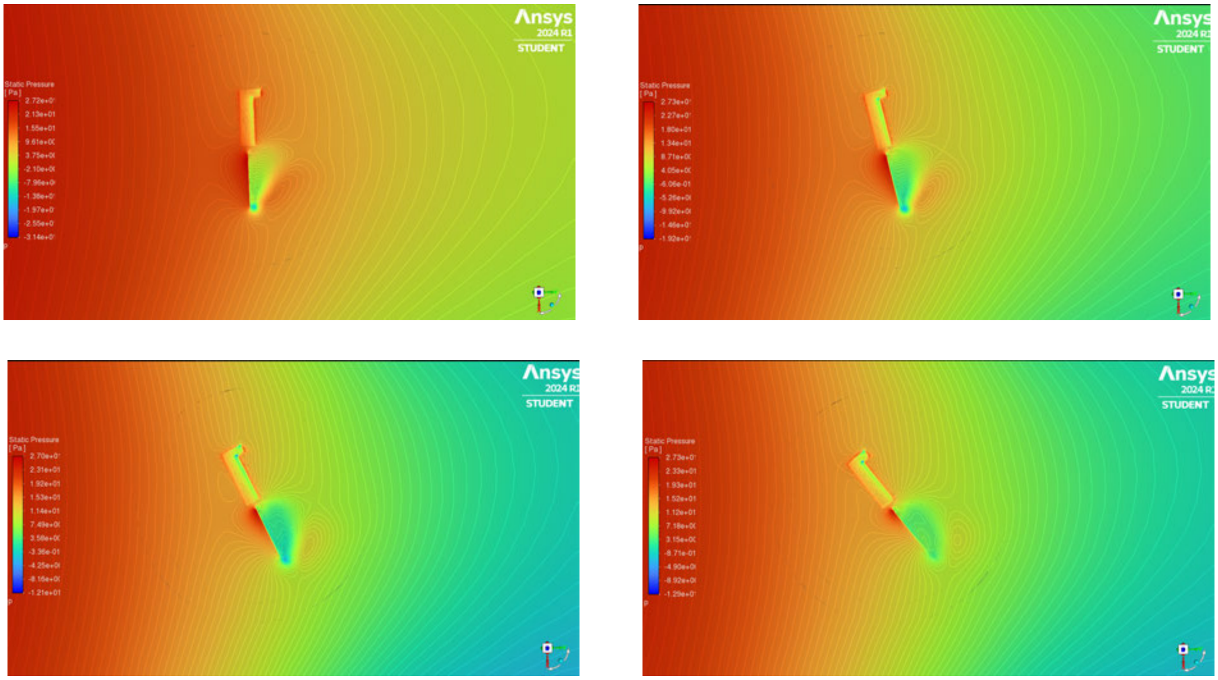

Figure 3.39: Blade-profile (d) (G4) pressure contours @ $v = 2.71\ m/s$ & $\lambda = 0.9$

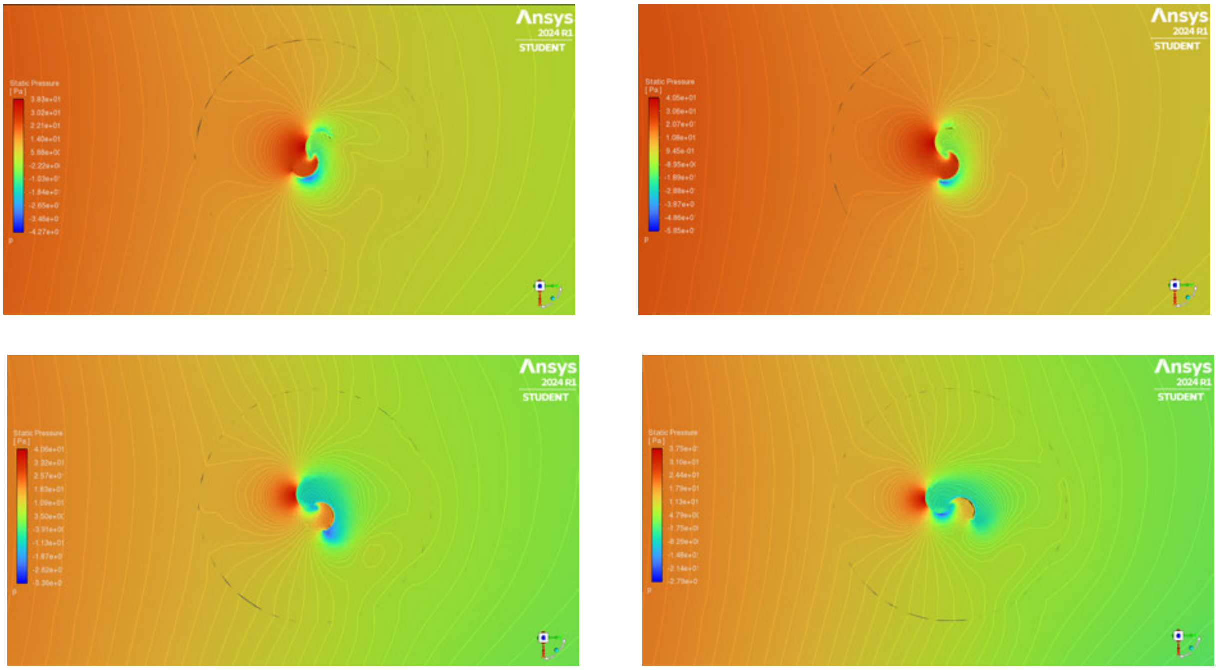

Figure 3.40: Savonius pressure contours @ $v = 2.71\ m/s$ & $\lambda = 0.9$

Chapter 4

Conclusions

4.1 Summary

Experimental studies of the novel S-WIND VAWT in the Complex Fluids Lab at Montclair State University were conducted after the design and construction of a wind-tunnel, properly scaled to match the dimensions of the lab. A small-scale prototype was provided by the creator and industrial designer, Sevdalin Semov, which was utilized for preliminary performance analyses across a number of different blade configurations. By placing the turbine at varying distances from a simulated wind-source i.e. a Dayton 2-Speed Fan, estimated varying inlet velocity conditions were calculated and tested. The small-scale model was placed at $D = 7ft$ from the fan, an anemometer is leveraged to measure instantaneous wind speeds over a selected time interval of $t_{exp} = 240s$ at both fan settings. The wind speed was averaged and utilized as an estimated inlet velocity conditions, $V_{tun} = (3.27 \text{ m/s}, 3.91 \text{ m/s})$. The S-WIND Prototype was connected via a gearwheel and belt to a 3-phase actuator from which Voltage and Current values may be extracted. A contact tachometer capable of capturing instantaneous values was utilized to capture loaded RPM across the same t_{exp}, for the (6, 8, 10) blade-numbers at the (Spiral, Staggered, Parallel) blade-configurations. The same is true of Voltage and Current with the use of a continuous data-collection Multi-meter as discussed in Chapter 2. It was found that the Parallel struggled to maintain consistent motion (RPM) under load at both inlet velocities, due to a lack of additional force per half-revolution and was dismissed after initial testing. The Spiral and Staggered configurations saw proportional increases in the maximum recorded loaded RPM value as the number of blades was increased at both inlet velocities; with the exception of the Staggered configuration tested at $v = 3.91$ m/s. This trend was however not largely consistent for the average loaded RPM at varying blade numbers. The Spiral configuration saw a proportional relationship between number of blades and average loaded RPM for both inlet velocities, however the Staggered configuration did not. Instead the 10-Blade Staggered performed the worst at higher inlet velocity of $v = 3.91$ m/s, however at the slower inlet velocity of $v = 3.27$ m/s, the Staggered configuration begins to shows some indication of a trend between 8 and 10-Blades. The Staggered may not be able to operate at higher wind speeds, as it is noted it's decrease in performance at the higher inlet velocity, and higher fluctuations in turbine loaded RPM. The Spiral configuration displays further interest, and has similarities to a helical-Savonius, potentially eliminating the high cost of producing twisted blades, and instead simply applying a set-fixed angular spacing between stacked blade-pairs.

Numerical studies of the novel S-WIND VAWT explored single-blade pair arrangements of four varying blade-profiles proposed by Mr. Semov for preliminary aerodynamic performance analyses. An equivalent-scale Savonius geometry was also constructed to serve as a comparative analyses, and was verified through results of previous studies. Geometries of the blade-profiles were designed with the use of Autodesk Fusion 360 [18], and simulations were constructed with the use of Ansys ® Fluent Student 2024 R1 [9]. The simulation domain and appropriate fluid zones were created with the use of Ansys ® DesignModeler [8], meshing was completed in Ansys ® Mesh [10]. Mesh refinements were performed on each blade-profile, with size alterations applied to blade faces and edges, and 15 maximum inflation layers. The overall mesh element-count for the blade profiles in respective order of the blade-profiles (G1, G2, G3, G4, Sav.) was (993394, 1013399, 996822, 994322, 1036949). In Ansys ® Fluent Student 2024 R1, the multiple reference frame model is utilized to create a steady-state solution for all blade-profiles to act as an initial flow field for the transient case with a sliding mesh. The steady-state solution had stabilized values for all reported quantities and nearly all error residuals fell below $1 \cdot 10^{-5}$. A time-step analysis is conducted, comparing the transient solution values over one full turbine revolution at time-step values in the set, $\Delta T = (0.1s,\ 0.05s,\ 0.01s,\ 0.005s,\ 0.001s)$. The smallest recorded time-step, although captures a finer representation of the model's behavior, takes $>$ 8hrs. to complete one-revolution over $\sim$ 17000 iterations. The time-step selected in this analysis was $\Delta t = 0.05s$, due to a relative η % error of $\leq 5\%$ to solution-values of $\Delta t = 0.001s$, and because of the vast number of simulations (40+) that were required to be run. An aerodynamic performance analysis was performed by prescribing various values of ω to the blade-profiles to simulate power efficiency estimates at desired tip-speed ratios of: λ = (0.3, 0.6, 0.9, 1.2). The utilized approaches have their limitations, most considerably being that both the MRF and Sliding Mesh are assuming constant inlet velocities v, as well as constant *prescribed* rotational velocities ω for turbine speeds. However, the simulation setup process utilizing the MRF and Sliding Mesh model is well studied and verified across a number of varying simulated wind turbine studies. The efficiency of the created Savonius geometry, $\eta_{sav} = 0.1390$ @ $\lambda = 0.9$ aligns within ranges of previous findings in ([2], [21], [20]), and the created S-WIND simulations are within range of the Savonius. It is found that blade-profile (b) (G2), is considered to be the 'optimal' blade-profile amongst the observed geometries, with a maximum efficiency $\eta = 0.1752$ @ $\lambda = 0.6$, exceeding the originally proposed blade-profile (a) (G1), and the comparative Savonius; but not particularly exceeding its maximum capacity as shown in Figure 2.1. Blade-profile (b) achieves the highest value for η, because of its ability to generate large values of torque, while also achieving a high angular velocity (ω). Simulation optimization-processes could and should be performed in terms of: mesh quality improvement, blade AoA refined behavioral modeling, assurance of proper fluid domain sizing, and hub-region improvement. The proposed S-WIND geometry in this research could not have been simplified to a 2D simulation without significant reductions in accuracy in both proper geometry representation and solution values.

4.2 Further Considerations

Flow-Driven Simulations Flow-Driven Simulations are also an area of interest to acquire more realistic determinations on a turbine's real-world performance. To do so, this would require the utilization of Ansys ® Fluent's Six Degrees of Freedom Solver in order to have the wind drive the turbine's motion, as opposed to prescribing a rotating region a rotational velocity (ω).

Multi-Blade Pair Configurations Future studies may explore simplifying the full-turbine geometry to not include a flap-region, to not include a hub (unchanged from current conditions), and to implement obstacles in place of the segment of the returning blades on the DW and LW portion of the configuration's revolution; or contain the flow domain to only include the region of interest as done in [2] in order to potentially model stacked blade-pairs i.e. full-turbine configurations.

Array Configurations An original motivation for analysis on VAWTs stemmed from the findings within [16], on the potential for lift-based VAWT arrays to perform up to an order of magnitude greater than that of HAWT arrays. An expansion of this research is an area of interest, not necessarily pertaining to the S-WIND VAWT. This would require the ability to model fully-functional turbines, unless a single-blade pair array would be considered as a simpler problem.

Mesh Improvements Additional considerations can be made to look into methods for acquiring further licensing past the general student version of Ansys ® 2024 Student Fluent for mesh improvement. 3D-CFD analyses recommend far more than the limited 1,048,000 mesh elements and this would improve solution results considerably. However, under limitations of the student mesh, suggestions have been made to utilize the Fluent-specific Meshing module in [9] instead of the standalone Mesh module. This will likely lead to improved mesh quality results. Within the Fluent standalone Mesh module however, the removal of the mesh inflation layers proved to display significant mesh quality improvement, and was tested after determining Blade-Profile (b) to be an ’optimal’ configuration; thus considerations for the removal or alteration of the set-up for blade inflation layers can be made. Additional studies also demonstrate that quality results can be achieved for 3D-simulations, despite mesh limitations as seen in [13].

Bibliography

[1] A. Alaimo, A. Esposito, A. Messineo, and C. Orlando and D. Tumino, *3D CFD Analysis of a Vertical Axis Wind Turbine*, Energies 8 (2015) DOI: 10.3390/en8043013.

[2] N. Alom, U. Saha, *Four Decades of Research Into the Augmentation Techniques of Savonius Wind Turbine Rotor*, J. Energ. Res. Techn. 5 (2018) DOI: 10.1115/1.4038785.

[3] Ansys ® 2024 Fluent Theory Guide, R1, *Basic Fluid Flow*, 47-50, ANSYS, Inc.

[4] Ansys ® 2024 Fluent Theory Guide, R1, *Flows with Moving Reference Frames*, 20-24, ANSYS, Inc.

[5] Ansys ® 2024 Fluent Theory Guide, R1, *Flows using Sliding and Dynamic Meshes*, 35-40, ANSYS, Inc.

[6] Ansys ® 2024 Fluent Theory Guide, R1, *Turbulence*, (42, 68), ANSYS, Inc.

[7] Ansys ® 2024 Fluent User's Guide, R1, *Improving and Examining the Mesh and its Quality* 544-545, ANSYS, Inc.

[8] Ansys ® 2024 Student DesignModeler, R1, ANSYS, Inc.

[9] Ansys ® 2024 Student Fluent, R1, ANSYS, Inc.

[10] Ansys ® 2024 Student Mesh, R1, ANSYS, Inc.

[11] J. Araneo, B. J. Chung, M. Cristaldi, J. Pateras, A. Vaidya and R. Wulandana, *Experimental control from wake induced autorotation with applications to energy harvesting*, Int. J. Grn. Energ. 16 15 (2019) DOI: 10.1080/15435075.2019.1671413.

[12] M.M. Bashar, *Computational and Experimental Study on Vertical Axis Wind Turbine in Search for an Efficient Design*, (2014) Electronic Theses and Dissertations, 1184, URL: https://digitalcommons.georgiasouthern.edu/etd/1184.

[13] N. Bogdan, R. Allaire, *On the Three Dimensional Interaction between Flexible Fibers and Fluid Flow*, Fluids 2 (2017) DOI: 10.3390/fluids2010004.

[14] M. Borg, A. Shires, and M. Collu, *Offshore floating vertical axis wind turbines, dynamics modelling state of the art. part I: Aerodynamics*, Ren. Energ. Sust. Rev. 39 (2014) DOI: 10.1016/j.rser.2014.07.096.

[15] F. Castellani, D. Astolfi, M. Peppoloni, F. Natili, D. Buttà, and A. Hirschl, *Experimental Vibration Analysis of a Small Scale Vertical Wind Energy System for Residential Use*, Machines 7 (2019) DOI: 10.3390/machines7020035.

[16] J. Dabiri, *Potential order-of-magnitude enhancement of wind farm power density via counter-rotating vertical-axis wind turbine arrays*, J. Ren. Sust. Energ. 3 4 (2011) DOI: 10.1063/1.3608170.

[17] N. Franchina, G. Persico, and M. Savini, *2D-3D Computations of a Vertical Axis Wind Turbine Flow Field: Modeling Issues and Physical Interpretations*, Ren. Energ. 136 (2019) DOI: 10.1016/j.renene.2018.09.086.

[18] Autodesk Fusion ©2024, Student Plan, Autodesk, Inc.

[19] A.C. Hansen, *Yaw dynamics of horizontal axis wind turbines*, (1992) DOI: 10.2172/5406093.

[20] H. Saeed, A. M. Elmekawy, and S. Z. Kassab, *Numerical study of improving Savonius turbine power coefficient by various blade shapes*, 58 429-441 (2019) DOI: 10.1016/j.aej.2019.03.005.

[21] I. Pedzisz, P. Magryta, and K. Pietrykowski, *Computational Fluid Dynamics Studies of a Vertical Axis Wind Turbine with a Variable Swept Area*, Adv. Sci. Techn. Res. J. 18 2 (2024) DOI: 10.12913/22998624/185255.

[22] F. R. Menter, *Two-Equation Eddy-Viscosity Turbulence Models for Engineering Applications*, AIAA J. 32 8 1598-1605 (1994) DOI: 10.2514/3.12149.

[23] M.H. Mohamed, A.M. Ali, and A.A. Hafiz, *CFD analysis for H-rotor Darrieus turbine as a low speed wind energy converter*, Eng. Sci. Techn. Int. J. 18 (2015) DOI: 10.1016/j.jestch.2014.08.002.

[24] M.H. Mohamed, G. Janiga, E. Pap, and D. Thévenin, *Optimal blade shape of a modified Savonius turbine using an obstacle shielding the returning blade*, Energ. Cons. Mngmt. 1 52 (2011) DOI: 10.1016/j.enconman.2010.06.070.

[25] M. Nini, V. Motta, G. Bindolino, and A. Guardone, *Three-dimensional simulation of a complete Vertical Axis Wind Turbine using overlapping grids*, Comp. Appl. Math. 270 78-87 (2014) DOI: 10.1016/j.cam.2014.02.020.

[26] S. Semov, Project S-WIND Powerpoint, *Project S-WIND Conceptual Image*.

[27] D. W. Wekesa, C. O. Saoke and J. N. Kamau, *An experimental investigation into performance characteristics of H-shaped and Savonius-type VAWT rotors*, Sci. Afrc. 10 (2020) DOI: 10.1016/j.sciaf.2020.e00603.

[28] R.Whittlesey, *Chapter 10 - Vertical Axis Wind Turbines: Farm and Turbine Design*, Wind Energ. Eng. 185-202 (2017) DOI: 10.1016/B978-0-12-809451-8.00010-2.

[29] The United States Government, *Executive Order on Tackling the Climate Crisis at Home and Abroad*, The White House (2021) URL: https://www.whitehouse.gov/briefing-room/presidential-actions/2021/01/27/executive-order-on-tackling-the-climate-crisis-at-home-and-abroad.

[30] R.Wulandana, D. Foote, B. J. Chung, and A. Vaidya, *Vortex-induced autorotation potentials of bladeless turbine models*, Int. J. Grn. Energ. 19 2 (2022) DOI: 10.1080/15435075.2021.1941044.